remote sensing

MDPI

Article

Capacity of Satellite-Based and Reanalysis Precipitation Products in Detecting Long-Term Trends across Mainland China

Shanlei Sun [1,*], Wanrong Shi [1], Shujia Zhou [2], Rongfan Chai [1], Haishan Chen [1], Guojie Wang [3], Yang Zhou [1] and Huayu Shen [4]

1 Collaborative Innovation Center on Forecast and Evaluation of Meteorological Disasters/Key Laboratory of Meteorological Disaster, Ministry of Education/International Joint Research Laboratory on Climate and Environment Change, Nanjing University of Information Science and Technology (NUIST), Nanjing 210044, China; 20181201117@nuist.edu.cn (W.S.); rfchai@nuist.edu.cn (R.C.); haishan@nuist.edu.cn (H.C.); yangzhou@nuist.edu.cn (Y.Z.)
2 Jintan Meteorological Bureau, Changzhou 213200, China; 20191201122@nuist.edu.cn
3 School of Geographical Sciences, NUIST, Nanjing 210044, China; gwang@nuist.edu.cn
4 Ningbo Meteorological Bureau, Ningbo 315012, China; qxj@nbyz.gov.cn
* Correspondence: sun.s@nuist.edu.cn; Tel.: +86-025-5869-5622

Received: 23 July 2020; Accepted: 4 September 2020; Published: 7 September 2020

Abstract: Despite numerous assessments of satellite-based and reanalysis precipitation across the globe, few studies have been conducted based on the precipitation linear trend (LT), particularly during daytime and nighttime, when there are different precipitation mechanisms. Herein, we first examine LTs for the whole day (LT_{wd}), daytime (LT_d), and nighttime (LT_n) over mainland China (MC) in 2003–2017, with sub-daily observations from a dense rain gauge network. For MC and ten Water Resources Regions (WRRs), annual and seasonal LT_{wd}, LT_d, and LT_n were generally positive but with evident regional differences. Subsequently, annual and seasonal LTs derived from six satellite-based and six reanalysis popular precipitation products were evaluated using metrics of correlation coefficient (CC), bias, root-mean-square-error (RMSE), and sign accuracy. Finally, metric-based optimal products (OPs) were identified for MC and each WRR. Values of each metric for annual and seasonal LT_{wd}, LT_d, or LT_n differ among products; meanwhile, for any single product, performance varied by season and time of day. Correspondingly, the metric-based OPs varied among regions and seasons, and between daytime and nighttime, but were mainly characterized by OPs of Tropical Rainfall Measuring Mission (TRMM) 3B42, ECMWF Reanalysis (ERA)-Interim, and Modern Era Reanalysis for Research and Applications (MERRA)-2. In particular, the CC-based (RMSE-based) OPs in southern and northern WRRs were generally TRMM3B42 and MERRA-2, respectively. These findings imply that to investigate precipitation change and obtain robust related conclusions using precipitation products, comprehensive evaluations are necessary, due to variation in performance within one year, one day and among regions for different products. Additionally, our study facilitates a valuable reference for product users seeking reliable precipitation estimates to examine precipitation change across MC, and an insight (i.e., capacity in detecting LTs, including daytime and nighttime) for developers improving algorithms.

Keywords: precipitation; reanalysis; satellite; linear trends; mainland China

1. Introduction

Precipitation is a critical hydrometeorogical variable that plays a key role in energy and water cycles, and thus impacts the weather, climate, hydrology, ecosystem, and Earth system [1–3]. Precipitation

is closely bound to life on Earth, due to it being the major source of freshwater [4]. As a result, its measurement is the focus for various disciplines (e.g., atmospheric sciences, ecology, hydrology, agriculture, and economy), in spite of their differences [2,5–7]. For instance, continuous and long-term precipitation observations are necessary for scientific research, but also for informing policy-makers of suitable measures to mitigate the adverse impacts of climate change, especially for droughts and floods [8–12]. Despite its exceptional importance, there still exist great challenges related to obtaining reliable precipitation observations with a long enough time span and large enough space coverage [13–15].

It is well-known that the most direct pathway to obtain precipitation data is through in situ measurements with different gauges (e.g., tipping-bucket rain gauges; [16]). Gauge observations have been extensively utilized by different sectors (e.g., agriculture, industry, and forestry), and have greatly promoted precipitation-related scientific disciplines, e.g., climate studies [10,17,18]. Despite that, we should note that gauges are related to high variability of the rain-bearing systems at different spatio-temporal scales and have an uneven spatial distribution [19,20]. These factors limit the representativeness of gauge precipitation observations to a large extent, and introduce uncertainty into gauge data-based conclusions. With the development of radar technology over past decades, technologically-sophisticated precipitation algorithms based on radar radiance signals have been developed and various corresponding precipitation estimates have been proposed [21–23]. Radar-based precipitation products undoubtedly have the potential to solve or at least reduce the limitations of gauge measurements; for example, they have a more extensive coverage and higher spatio-temporal resolution, which are critical for the analysis of hydrometeorological processes, especially extremes such as flash floods and droughts [2,24]. However, considering the high installation and maintenance costs of radars, the shorter time span of radar observations, and topography-induced radar blockage, radar-based precipitation products are limited and unavailable for some regions, e.g., the nearly negligible radar estimates overseas [14,22,25].

Recently, satellite technology and numerical models/reanalysis systems have developed significantly; therefore, satellite-based precipitation retrievals and precipitation estimates from the models/reanalysis systems have become increasingly attractive and available [3,5,26–31]. Satellite-based precipitation data are derived using various statistical and/or physics-based retrieval algorithms with the radiance information from the satellite-carried sensors, including VIS/IR sensors on geostationary (GEO) and low Earth orbit (LEO) satellites, and passive (PMW) and active MW sensors on LEO satellites. Satellite-based products generally include three types, i.e., VIS/IR- and MW-based estimates, and data through combining the VIS/IR and MW information. Examples include the Tropical Rainfall Measuring Mission (TRMM) Multi-Satellite Precipitation Analysis (TMPA) from the National Aeronautics and Space Administration (NASA) Goddard Space Flight Center (GSFC; [32]), the Precipitation Estimation from Remotely Sensed Information Using Artificial Neural Networks (PERSIANN; [33,34]), the PERSIANN-Cloud Classification System (CCS; [13,35]), the PERSIANN-Climate Data Record (CDR; [25]), the Global Satellite Mapping of Precipitation (GSMaP) Microwave-Infrared Combined Reanalysis (RNL; [32,36]) of the Earth Observation Research Center (EORC) of the Japan Aerospace Exploration Agency (JAXA), the National Oceanic and Atmospheric Administration (NOAA) Climate Prediction Center (CPC) morphing technique (CMORPH; [37]), the Integrated Multi-satellite Retrievals for Global Precipitation Measurement (IMERG; [38]), the Climate Hazards Group InfraRed Precipitation with Station Data (CHIRPS; [39]), and a new global Multi-Source Weighted-Ensemble Precipitation (MSEWP) rainfall dataset [40]. Notably, satellite-based precipitation products can only be dated back to the beginning of the satellite era. As an important alternative, reanalysis precipitation data, which are simulated using new atmospheric models combined with advanced data assimilation systems [41–45], provide a means to fulfill the specific requirements (i.e., centennial and even longer precipitation records) of the studies. Additionally, reanalysis systems provide the nearly realistic atmosphere circulation fields, which makes it possible to do many things, including understanding precipitation changes from the perspective of atmospheric dynamical mechanisms [46–48]. The most frequently used reanalysis precipitation datasets include the National Centers for Environmental Prediction

reanalysis (NCEP1 and NCEP2; [42,43]), NCEP Climate Forecast System Reanalysis (CFSR; [49]), ECMWF Reanalysis-5 (ERA-5; [46]) and ERA-Interim [41], the Japanese 55-year Reanalysis Project (JRA-55; [44]), and the National Aeronautics and Space Administration (NASA) Modern Era Reanalysis for Research and Applications (e.g., MERRA-2; [45]).

Before using these products, it is of paramount importance to determine the reliability of the precipitation products using dependable reference datasets, because the inherent uncertainties within these products would likely affect final results, adversely impacting confidence levels [42,50–56]. In terms of a study's specific needs and goals, the satellite-based and reanalysis precipitation datasets have been widely evaluated at different spatio-temporal scales with a series of validation metrics (e.g., [6,50,56–68]). For instance, Sun et al. [6] selected several continuous and categorical validation statistics combined with bias and error decomposition techniques to assess the performance of the PERSIANN-Climate Data Record (CDR) precipitation product in the Huai River Basin, China, and pointed out that the daily, monthly and annual performance of this product varied in accordance with obvious intra-annual cycles. Huang et al. [62] systematically assessed five satellite-based precipitation products (CMORPH, PERSIANN and TRMM3B41RT, TRMM3B42RT, and TRMM3B42) with observations at 2400 weather sites across China, and found that estimates generally captured the overall spatial-temporal variation of precipitation, especially for warm seasons and humid regions. Beck et al. [40] compared 22 gridded daily precipitation datasets across the globe during 2000—2016 with daily observations at 76086 gauges and hydrological modeling, and highlighted that there existed large differences in the accuracy of precipitation estimates and more attention should be paid for precipitation dataset selection in both research and operational applications. de Leeuw et al. [65] used the daily precipitation observations from England and Wales to evaluate the ERA-Interim products, and found that this dataset underestimated the observations on a daily scale, while it could capture the statistics of extreme precipitation events. Lorenz and Kunstamann [67] analyzed the hydrological cycle with three state-of-the-art reanalyses (ERA-Interim, MERRA-2, and CFSR), and demonstrated that large differences existed between the reanalyses and the observations.

The previous evaluations have provided valuable information for the theoretical understanding and improvement of satellite-retrieved algorithms and reanalysis systems. Nonetheless, most were conducted using daily, monthly and annual reference precipitation data; thus, the information about the capacity of the satellite-based and reanalysis precipitation is scarce on a sub-daily scale, especially for China. In fact, there are evident differences in the mechanisms of precipitation within one day, which are closely related to thermodynamic and dynamic processes of water and energy fluxes [3,69–74]. For example, results from Yu et al. [74] indicated that long-duration stratiform precipitation frequently occurred in the early morning during the warm season over central-eastern China, while the late afternoon experienced a higher frequency of short-duration convective precipitation. Therefore, evaluating the multi-source precipitation products with sub-daily observations (daytime and nighttime datasets at least) could provide more detailed information, e.g., flexibility for a precipitation product on sub-daily scale. This is very useful to further improve satellite-based algorithms and models/reanalysis systems from the perspective of sub-daily precipitation mechanisms, and even correct the precipitation products using the sub-daily rather than daily measurements. Additionally, sub-daily precipitation changes have become a hot topic in current research, and numerous studies have been conducted (e.g., [71,75–82]). Cheng et al. [71] pointed out that on annual and seasonal scales (except during spring), the majority of meteorological station records (1961–2006) of Southwest China displayed downward trends for total, daytime, and nighttime precipitation. Lin et al. [80] analyzed characteristics of summer precipitation diurnal variations during 2001–2014 in the Hubei Province of China, and suggested that the diurnal variations existed obvious regional differences. Based on observational day and night precipitation during 1961–2005 across Xinjiang, China, Han et al. [81] concluded that the annual increasing trends of precipitation in the daytime and nighttime respectively accounted for 49% and 51% of the total increasing trend in annual precipitation. Liu et al. [82] found that with the CMORPH dataset during 2008–2014, both the daytime and nighttime precipitation were detected to increase in

summer over the Qilian Mountains, China. Lenderink et al. [77] reported that hourly precipitation extremes have substantially increased in the last century over De Bilt, Netherlands, and Hong Kong, China. Thus, an issue arises—can the existing precipitation products capture the linear trends on a sub-daily scale based on different validation metrics? This question has been paid little attention (e.g., [83]), despite the basis to examine precipitation trends with these datasets. Thus, assessments regarding precipitation trends can provide fundamental information to select the reliable products for exploring precipitation changes, particularly for regions with limited or even no observations (e.g., West China in Figure 1).

Considering the gaps in the previous works of precipitation evaluations, we used China as an example to examine the multi-source precipitation products' capacity to detect precipitation linear trends during daytime and nighttime. Thus, the main objectives of this work were to (1) investigate the spatial distribution of precipitation changes using daily, daytime, and nighttime records from 2393 weather sites across China; (2) to quantify the performance of selected products (i.e., six satellite-based and six reanalysis datasets) in detecting precipitation trends on a sub-daily scale with different validation metrics (correlation coefficient, bias, root mean square error, and sign accuracy) through a comparison with gauge observations; and (3) to identify the metric-based optimal products at a sub-daily scale.

2. Data and Methodology

2.1. Data

2.1.1. Observed Precipitation

To evaluate the capabilities of various products in capturing precipitation changes, sub-daily (i.e., daytime, P_d, 0000–1200 UTC; and nighttime, P_n, 1200–2400 UTC) accumulated precipitation data observed from 2003 to 2017 at 2481 weather sites across China (Figure 1), including basic, benchmark, and general meteorological stations, were collected from the China Meteorological Administration (CMA). Although both datasets had undergone a series of quality control measures and homogenization, e.g., outlier identification, internal consistency checks, and spatio-temporal consistency checks [84], there were still missing values within the records. Therefore, to maximize the observational information, we processed the datasets following the procedures described below. First, the number of daytime and nighttime values was computed for each year at each site. If the days with missing values for daytime or nighttime observations exceed 50 at a site, the site was removed. Secondly, for the remaining sites, the bilinear interpolation method was employed to fill the missing values with the observations at the two closest sites. There were 2393 sites remaining after this process (Figure 1), and the accumulative precipitation for a whole day (abbreviated as P_{wd}) was then obtained as the sum of P_d and P_n.

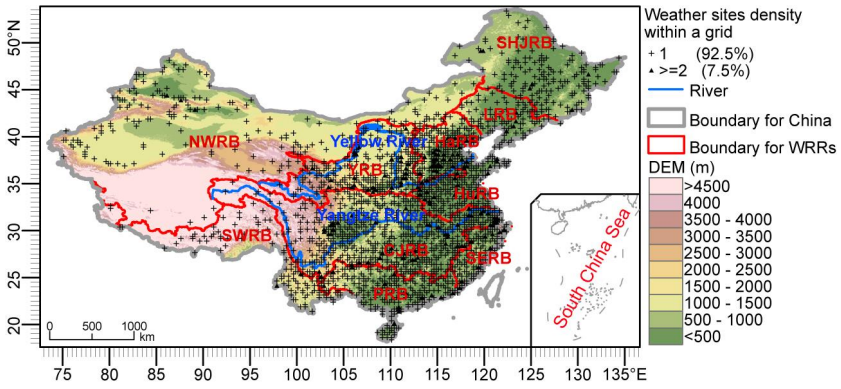

Figure 1. Geographic distribution of the selected 2281 grids (0.25° × 0.25°), at least corresponding to a weather site. The digital elevation model (DEM) with a spatial resolution of 90 m is available at http://srtm.csi.cgiar.org/. [85] Crosses and triangles correspond to 1 and more than 2 sites within a given grid, respectively, followed by the percentage of grid shown in the bracket.

China is located in a typical monsoon region (i.e., the East Asian monsoon region), with evident spatio-temporal variability of precipitation and the related mechanisms [86]. Mainland China (MC) is divided into ten Water Resources Regions (WRRs, Figure 1), which is beneficial for examining regional differences in the performance of each product to detect precipitation trends. We conducted annual and seasonal evaluations of P_{wd}, P_d, and P_n trends during 2003–2017 on national and regional (i.e., MC and WRR, respectively) scales. Here, spring, summer, autumn, and winter were specified as March–May, June–August, September–November, and December–February, respectively.

2.1.2. Satellite-Based and Reanalysis Precipitation Datasets

In this study, considering the precipitation datasets availability and time span (study period of 2004–2017), we collected twelve sets of gridded precipitation data, including six satellite-based and six reanalysis products, for evaluation. Detailed information of these datasets is shown in Table 1. Of the selected satellite-based precipitation products, both the TRMM (i.e., TRMM3B42RT and TRMM3B42 adjusted with gauge observations), and the GSMaP (i.e., GSMaP-RNL and GSMaP-RNLG adjusted with gauge observations) precipitation datasets are produced through merging VIS/IR and MW information but are based on different algorithms [32,36]. In contrast, PERSIANN and PERSIANN-CCS belong to the VIS/IR family of satellite-based precipitation products [13,33–35,87]. The main differences in the two PERSIANN products are that the PERSIANN-CCS system enables the categorization of cloud-patch features based on cloud height, areal extent, and variability of texture estimated from satellite imagery, which is optimized for observing extreme precipitation, particularly at a very high spatial resolution. The six reanalysis precipitation products include JRA-55, ERA-Interim, ERA-5, NCEP1, NCEP2, and MERRA-2. These reanalysis products are produced based on different forecasting systems by assimilating many of the basic surface and upper-atmospheric fields from multiple sources, e.g., the surface humidity, radiosonde-based specific humidity, wind fields, and satellite-derived radiance. Among them, different data assimilation techniques are employed. For example, the ERA-Interim, ERA-5, and JRA-55 adopt four-dimensional variational (4D-VAR) data assimilation systems, whereas the MERRA-2, NCEP1, and NECEP2 utilize 3D-VAR assimilation systems. For more details about these datasets, the reader can refer to the product-specific user guide and the related literature.

Table 1. Summary of the selected satellite and reanalysis rainfall products.

Products	Spatial Resolution and Space Span	Temporal Resolution and Time Span	Bias Correction	Assimilation System	References
TRMM-3B42RT (V7)	0.25° × 0.25°, 50° S–50° N	2000 to present, 3-hourly	No	/	[32]
TRMM-3B42 (V7)	0.25° × 0.25°, 50° S–50° N	2000 to 2017, 3-hourly	Corrected with GPCP, and CAMS	/	[32]
PERSIANN	0.25° × 0.25°, 60°S–60°N	2000 to present, 3-hourly	No	/	[34]
PERSIANN-CCS	0.04° × 0.04°, 60° S–60° N	2003 to present, 3-hourly	No	/	[35]
GSMaP-RNL (V6)	0.1° × 0.1°, 60° S–60° N	2000 to present, hourly	No	/	[36]
GSMaP-RNLG (V6)	0.1° × 0.1°, 60° S–60° N	2000 to present, hourly	Corrected with CPCU	/	[36]
JRA-55	1.25° × 1.25°, Global	1958 to present, 3-hourly	No	4D-VAR	[44]
ERA-Interim	0.75° × 0.75°, Global	1979 to present, 3-hourly	No	4D-VAR	[49]
ERA-5	0.25° × 0.25°, Global	1979 to present, 3-hourly	No	4D-VAR	[46]
NCEP1	1.875° × 1.875°, Global	1948 to present, 6-hourly	No	3D-VAR	[42]
NCEP2	1.875° × 1.875°, Global	1979to present, 6-hourly	No	3D-VAR	[43]
MERRA-2	0.5° × 0.667°, Global	1980 to present, hourly	Corrected with CPCU or CMAP/GPCPv2.1	3D-VAR	[45]

Note: CPCU: the NOAA Climate Prediction Center (CPC) Unified Gauge-Based Analysis of Global Daily Precipitation (CPCU) product. CMAP/GPCPv2.1: the CPC Merged Analysis of Precipitation (CMAP)/Global Precipitation Climatology Project product, version 2.2. GPCC: Global Precipitation Climatology Centre. CAMS: Climate Assessment and Monitoring Systems.

As shown in Table 1, datasets had different temporal and spatial resolutions, so it is necessary to process them before evaluation. First, the satellite-based and reanalysis P_d and P_n were summed from the 1-hourly, 3-hourly, or 6-hourly accumulated precipitation at product-specified grids. Then, based on the bilinear interpolation method, the P_d and P_n for all products (except for TRMM-3B42RT, TRMM-3B42, PERSIANN, and ERA-5) were resampled to the spatial resolution of 0.25°. This was mainly because most products correspond to a spatial resolution of 0.25° or higher, so the resampling-induced uncertainties could be reduced to some extent. For P_{wd}, its values were obtained using the sum of P_d and P_n from the resampled maps. The grids with at least one site were extracted to conduct performance evaluations. If any grid included more than one site, the average precipitation value at these sites was calculated to represent the final reference value of that grid.

2.2. Methodolody

The precipitation trends were calculated using

$$y = at + b \tag{1}$$

where y is annual or seasonal accumulative precipitation; t refers to time; a represents the slope coefficient, namely, linear trend; and b is the constant. Pearson's correlation and the two-tailed Student's t test (i.e., $p < 0.05$) were applied to check for statistically significant relationships.

Satellite-based and reanalysis precipitation trends were quantitatively assessed with the metrics of bias (B), which measured the trend differences between the products and the gauge observations; root mean square error (RMSE), which represented the overall accuracy of the trends derived from the products; the correlation coefficient (CC), which quantified the spatial consistency of the trends derived from the products; and accuracy of sign (AS), which examined the degree of agreement between the positive or negative sign of precipitation trends from the products and the observed data. These metrics were calculated using the following equations:

$$\mathrm{B} = \overline{a_P} - \overline{a_O} \tag{2}$$

$$\mathrm{RMSE} = \sqrt{\frac{1}{N}\sum_{i=1}^{N}\left(a_{O,i} - a_{P,i}\right)^2} \tag{3}$$

$$\mathrm{CC} = \frac{\sum_{i=1}^{N}\left(a_{O,i} - \overline{a_O}\right)\left(a_{P,i} - \overline{a_P}\right)}{\sqrt{\sum_{i=1}^{N}\left(a_{O,i} - \overline{a_O}\right)^2 \sum_{i=1}^{N}\left(a_{P,i} - \overline{a_P}\right)^2}} \tag{4}$$

$$\mathrm{AS} = \frac{nP}{nG} \tag{5}$$

where $a_{P,i}$ and $a_{O,i}$ represent the linear trends from a certain precipitation product and the gauge observation at the ith grid, respectively; N is the number of the used grids for evaluation across MC or each WRR; $\overline{a_P}$ and $\overline{a_O}$ represent the products and the observed trends averaged at the grids within MC or a certain WRR, respectively; and nP is the number of the grids, where the examined products shows the same sign of precipitation (e.g., P_{wd}, P_d or P_n) changes as the observed within a given region, but nG indicates the total number of grids in the region.

Considering the co-variation of P_d and P_n, we defined a joint AS (JAS), which represented the capacity of a given product to rightly detect the signs of both P_d and P_n changes relative to the observed data. JAS can be calculated by

$$\mathrm{JAS} = \frac{nP_{co}}{nG} \tag{6}$$

where nP_{co} is the number of the grids in which the signs of both P_d and P_n changes derived from the products are the same as those observed in a given region.

3. Results

3.1. Gauge Precipitation Changes across MC

Figure 2(a1) depicts observed annual LTs for MC and ten WRRs during 2003–2017. For MC, annual LT_{wd} and LT_d were 8.42 mm/yr ($p < 0.05$) and 4.96 mm/yr ($p < 0.05$), respectively, followed by an insignificant LT_n of 3.46 mm/yr. Comparing LT_{wd}, LT_d, or LT_n (i.e., signs and magnitudes) among WRRs, there were evident regional differences, while significant ($p < 0.05$) and larger increases (>13 mm/yr, >8 mm/yr and >7 mm/yr for LT_{wd}, LT_d and LT_n, respectively) were found in YZRB, SERB, and PRB, followed by the largest reductions (–13.95 mm/yr for LT_{wd}, −4.68 mm/yr for LT_d and −9.27 mm/yr for LT_n) in HuRB. In spring (Figure 2(b1)), LTs for WRRs and MC were between −4 mm/yr and 4 mm/yr, with the exceptions of SERB and PRB, which showed $LT_{wd} > 8$ mm/yr, and LT_d and LT_n > 4 mm/yr. During summer, MC LT_{wd} and LT_d (LT_n) were positive (negative) with a rate <2 mm/yr (Figure 2(c1)). Among ten WRRs, most exhibited smaller LT_{wd} (LT_d and LT_n) in summer, generally corresponding to between −3 mm/yr and 4 mm/yr (between −1.50 mm/yr and 2.50 mm/yr); however, significant ($p < 0.05$) decreasing and increasing LTs were detected over HuRB and YZRB (excluding LT_n) and SERB, and the LT_{wd}, LT_d, and LT_n were >6 mm/yr and > 4 mm/yr, respectively. As shown in Figure 2(d1), MC LT_{wd} and LT_d (LT_n) were 5.60 mm/yr ($p < 0.05$) and 2.80 mm/yr ($p < 0.05$), respectively. Except for two WRRs (i.e., HaRB and YRB), autumn LT_{wd}, LT_d, and LT_n were consistently positive from 2003 to 2017. However, magnitudes of autumn LTs differed among these WRRs, for which significant ($p < 0.05$) and larger increases (>8 mm/yr for LT_{wd} and 3.20 mm/yr for LT_d and LT_n) occurred in YZRB, SERB, and PRB. Regarding winter precipitation (Figure 2(e1)), SERB and PRB exhibited the highest LT_{wd} (>2.80 mm/yr) and LT_d and $LT_n > 0.90$ mm/yr, followed by the remaining WRRs and MC with an $LT_{wd} < 1.50$ mm/yr (LT_d and $LT_n < 0.70$ mm/yr). Additionally, comparing signs and magnitudes of LT_d and LT_n (Figure 2(a1–e1)), 10 and 15 of 55 cases (i.e., 11 (MC + 10 WRRs) × 5 (annual + seasonal scales)) showed opposite signs and larger differences, with ratios between LT_d and $LT_n > 2.00$ and < 0.50, respectively. These findings imply that LT_d and LT_n values were not consistent, possibly due to the different precipitating mechanisms during daytime and nighttime, and thus further confirms the necessity to evaluate various precipitation products at a sub-daily scale.

As shown in Table 2 and Figure 2(a2), 33% of grids had decreasing annual LT_{wd} across MC, generally in east LRB, HuRB, the YRB–YZRB border, and most of SWRB and NWRB. Moreover, 3% of grids in north-central HuRB showed significant ($p < 0.05$) negative annual LT_{wd} with a rate of −12 mm/yr. In contrast, 11% of grids had significantly ($p < 0.05$) increasing LT_{wd}, mainly situated in east SHRB, central YRB, northeast YZRB, north SERB, and middle PRB, for which LT_{wd} over the three latter regions exceeded 20 mm/yr. For both annual LT_d and LT_n (Table 2), negative values were found in > 30% of grids, followed by < 4% of grids with significant ($p < 0.05$) values. Moreover, in spite of smaller magnitudes of difference compared to annual LT_{wd}, similar spatial distributions for LT_d and LT_n were detected (Figure 2(a3,a4)). Figure 2(b2–b4,c2–c4,d2–d4,e2–e4) illustrate the spatial distribution of seasonal LT_{wd}, LT_d, and LT_n during 2003–2017. In broad terms, LT_{wd}, LT_d, or LT_n spatially differ during seasons, while in a given season, a generally similar spatial pattern is observed among LT_{wd}, LT_d, and LT_n, including for locations with significant ($p < 0.05$) LTs. For example, spring LT_{wd}, LT_d, and LT_n were negative at 30% of grids, primarily in NWR, SWRB, west YZRB, north HuRB, and HaRB (Figure 2(b2–b4) and Table 2); moreover, 2% of grids with significant ($p < 0.05$) changes were sporadically distributed, and larger reductions (–6 mm/yr for LT_{wd}, but –2 mm/yr for LT_d and LT_n) were in south SWRB. At the remaining grids, 60% of grids with larger increases for LT_{wd} (12 mm/yr), LT_d and LT_n (4 mm/yr) in spring for were mainly located in east YZRB, PRB, and SERB, and 5% of grids with significant ($p < 0.05$) changes were generally in SHRB–LRB, YRB–YZRB borderlands, and east PRB. As shown in Figure 2(c2–c4) and Table 2, 44% of grids with a negative summer LT_{wd}, LT_d, and LT_n were generally situated in central SHRB, LRB, HuRB, YRB–YZRB borderlands, west YZRB, PRB, and north SWRB, and the largest and significant ($p < 0.05$) reductions (−10 mm/yr) in 5% of grids were concentrated in HuRB. Of the remaining grids (>50%), the largest (10 mm/yr) and significant

($p < 0.05$) summer LTs were detected in 4% of grids mainly in northeast YZRB and north SERB. In autumn (Figure 2(d2–d4) and Table 2), LT_{wd}, LT_d, and LT_n were at least -6 mm/yr at 30% of grids in south LRB, YRB–HaRB–HuRB and YRB–YZRB borderlands, central NWRB, and central SWRB. Of the grids with increasing LTs, 14% of grids with large (10 mm/yr) and significant ($p < 0.05$) values were situated in central SHRB, central PRB, east YZRB, parts of middle YZRB (i.e., Sichuan basin), and SERB. During winter (Figure 2(e2–e4) and Table 2), there was an approximately equal balance of grids with negative and positive LT_{wd}, LT_d, or LT_n, which was generally 4mm/yr or −4mm/yr at most grids; moreover, increasing LTs were widely distributed across east coastal WRRs, south SWR, and central YRB. Furthermore, 2% of grids with significant ($p < 0.05$) increases in winter precipitation were patchily distributed across MC.

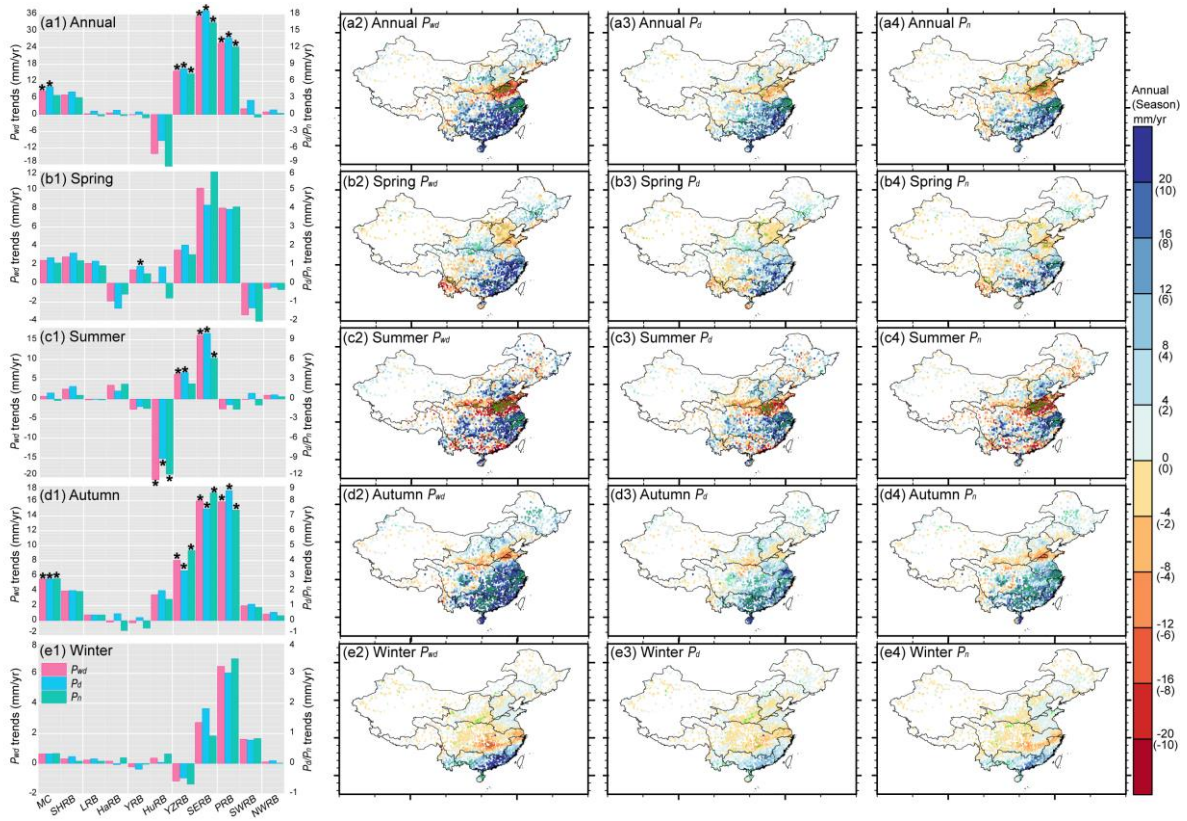

Figure 2. Linear trends (LTs) for mainland China (MC), ten Water Resources Regions (WRRs), and 2281 grids during 2003–2017. Annual and seasonal LTs averaged over MC and ten WRRs are shown in (**a1**) and (**b1**–**e1**), respectively, in which stars represent significant changes with $p < 0.05$. (**a2**) and (**b1**–**e2**) show spatial distributions of annual and seasonal P_{wd} trends across MC, respectively, with the green cross representing significant changes with $p < 0.05$. (**a1**–**e3**) and (**a1**–**e4**) are the same as (**a1**–**e2**), but for P_d and P_n trends, respectively.

Table 2. Percentage of grids with increasing and decreasing LTs across MC for the whole day (LT_{wd}), daytime only (LT_d), and nighttime only (LT_n).

	Annual			**Spring**			**Summer**			**Autumn**			**Winter**		
	LT_{wd}	**LT_d**	**LT_n**	**LT_{wd}**	**LT_d**	**LT_n**	**LT_{wd}**	**LT_d**	**LT_n**	**LT_{wd}**	**LT_d**	**LT_n**	**LT_{wd}**	**LT_d**	**LT_n**
Significant Increase	67	69	61	51	52	54	55	56	51	74	76	71	51	52	54
($p < 0.05$) Increase	11	11	9	6	6	5	6	6	4	17	14	17	3	2	3
Significant decrease	33	31	39	49	48	46	45	44	49	26	24	29	49	48	46
($p < 0.05$) Decrease	3	1	4	3	3	2	7	5	6	0	0	0	3	3	2

3.2. Evaluation Using Correlation Coefficient Metric

The CCs of LTs for the products and the observed values are depicted in Figure 3(a1–a5). For annual LTs, the corresponding CCs for TRMM3B42RT, TRMM3B42, PERSIANN, PERSIANN-CCS, and MERRA-2 were generally >0.40, suggesting that spatial distributions of annual LTs across MC can be derived from these products (Figure 3(a1)), especially for TRMM3B42 and MERRA-2 with CCs around 0.80. Besides, ERA-Interim, with an annual CC < 0.40, exhibited limited capacity in detecting annual LTs in space. However, annual CCs for the remaining six products were all below 0.10 and some were even negative, which indicates that these products are not able to capture the spatial distribution of LTs across MC. Comparing CCs of annual LT_d and LT_n, CC-based performance for each precipitation product differed over daytime and nighttime, especially PERSIANN-CCS and ERA-Interim, followed by TRMM3B42RT and PERSIANN. In spring (Figure 3(a2)), GSMaP-RNL, GSMaP-RNLG, JRA-55, ERA-55, NCEP1, and NCEP2 had negative CCs and therefore no ability to reflect the spatial distribution of LTs; however, the other products, with CCs > 0.40, had good performances, of which TRMM3B42 showed the best performances (CCs around 0.80) and the next was in TRMM3B42RT, PERSIANN, and MERRA-2 (CCs around 0.70). Furthermore, the spring CC-based performance of PERSIANN-CCS exhibited differences > 0.10 between daytime and nighttime. During summer (Figure 3a3), TRMM3B42 with CCs around 0.80 showed the best performance, followed by TRMM3B42RT and MERRA-2 (CCs around 0.70), ERA-Interim (CCs around 0.60), and PERSIANN and PERSIANN-CCS (CCs around 0.50). JRA-55, EAR-55, NCEP1, and NCEP2 with CCs < 0 indicated poor performance. Relative to spring, the capacity of GSMaP-RNL and GSMaP-RNLG to reproduce LTs in space increased in summer but was still limited, with CCs < 0.20. PERSIANN-CCS, GSMaP-RNL, and GSMaP-RNLG showed the greatest differences (>0.10) in summer CCs between daytime and nighttime. In autumn (Figure 3a4), the largest CCs (>0.80) were detected by TRMM3B42 and MERRA-2, while TRMM3B42RT, PERSIANN, and ERA-Interim had CCs ranging from 0.60 to 0.80. PERSIANN-CCS, JRA-55, and ERA-4 had CCs around 0.40 and could capture summer LTs spatially, while the remaining four products showed limited CC-based performance (CCs generally < 0.10). Comparisons of CCs for autumn LT_d and LT_n indicated that larger differences (>0.10) existed in PERSIANN, PERSIAN-CCS, JRA-55, and ERA-5, especially for the former three products with differences exceeding 0.20. Regarding winter CCs (Figure 3(a5)), eight of the products had values below 0.20 or 0, indicating that they had limited or no ability to capture winter LTs in space. Of the remaining products, the best product based on CC in winter was MERRA-2 (CCs around 0.90), followed by TRMM3B42 (CCs around 0.70), TRMM3B42RT (CCs around 0.50), and ERA-Interim (CCs < 0.40); no significant differences in CCs for LT_d and LT_n existed among these products.

To identify the CC-based optimal products (OPs) of LT_{wd}, LT_d, and LT_n, we compared CCs from the 12 examined products. The results are depicted in Figure 3(b1–b5). For MC, the annual, spring, summer, and autumn (excluding LT_d) CC-based OP for the three LTs was TRMM3B42, and the winter OP was MERRA-2. For annual cases (including the three LTs and ten WRRs), the CC-based OP for 17 of the 30 cases was MERRA-2, generally in northern WRRs, while 11 cases, including LTs for southern WRRs (excluding YZRB) and LT_d for LRB, HaRB, and YRB had an OP of TRMM3B42. In spring, the OP for more than ten cases was TRMM3B42, generally in southern WRRs, while 15 cases with the OP of MERRA-2 were in northern WRRs. With several exceptions (e.g., SHRB, HuRB, and NWRB) showing the summer OP of MERRA-2, TRMM3B42 was the OP in 16 cases. In winter, the OP for the overwhelming majority (27) of cases was MERRA-2, followed by three cases with ERA-Interim in SERB. Notably, some cases had CCs below 0.40 for the identified OPs, e.g., for LT_{wd}, LT_d, and LT_n in LRB and NWRB; this indicates that using the so-called CC-based OPs to represent spatial distribution of precipitation trends needs more caution in certain regions.

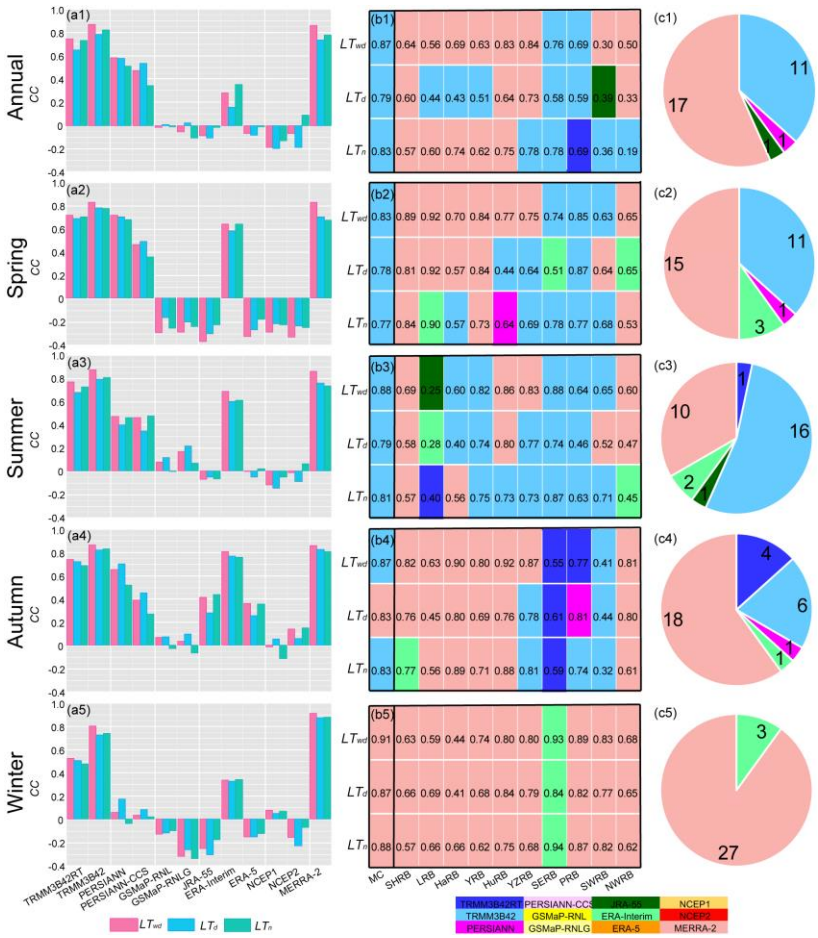

Figure 3. Correlation coefficients (CCs) for LTs from the selected 12 precipitation products (**a1**–**a5**), CC-based optimal products (OPs) for MC and ten WRRs (**b1**–**b5**), and number of cases corresponding to OPs for an annual or seasonal scale in ten WRRs (**c1**–**c5**). In figures (**b1**–**b5**), the number of each box represents the CC of the identified OP, which has been labelled with different colors. The number of figures (**c1**–**c5**) indicates the amount of a certain OP.

3.3. Evaluation Using Bias Metric

Figure 4(a1–a5,b1–b5) depict the percentage of grids with negative and positive Bs of annual and seasonal LTs across MC, respectively. For simplicity, we focused on analyses regarding negative Bs in this paragraph. More than 50% of grids had negative annual Bs for PERSIANN, PERSIANN-CCS, GSMaP-RNL, and GSMaP-RNLG products (Figure 4(a1)). In particular, PERSIANN LT_{wd} and LT_d had negative Bs in >65% of grids. With several exceptions (i.e., TRMM3B42, JRA-55, and MERRA-2 for LT_d; and NCEP1 for LT_n), annual Bs for the remaining products were negative in <50% of grids, and even TRMM3B42RT, ERA-Interim, and NCEP2 showed negative Bs in <35% of grids. As shown in Figure 4(a2), most products had negative spring Bs for LT_{wd} and LT_d in >50% of grids, especially for PERSIANN, ERA-Interim, and MERRA-2 with >65% of grids. However, six of the 12 products underestimated LT_n in around 50% of grids in spring, followed by the other six products with overestimations in >50% of grids. Similar to spring, >50% of grids with negative Bs for summer LT_{wd} and LT_d were detected by most of the products, of which PERSIANN, GSMaP-RNL, ERA-Interim, and NCEP2 corresponded to >65% of grids (Figure 4(a3)). Except for PERSIANN, summer LT_n was underestimated in <50% of grids by the products, particularly for JRA-55, ERA-Interim, and ERA-5 with a grid percentage < 25%. In autumn (Figure 4(a4)), despite several exceptions, >50% of grids had negative Bs for the three LTs, and the PERSIANN product had negative Bs in >70% of grids. Relative to autumn cases, the opposite happened during winter (Figure 4(a5)), i.e., percentages of grids with

negative Bs for LT_{wd}, LT_d, and LT_n being generally <50%, in particular for JRA-55 and ERA-Interim. In addition, based on percentages of grids with negative Bs for LT_d and LT_n (Figure 4(a1–a5)), differences generally exceeding 10% were identified on both annual and seasonal scales for most of products, particularly MERRA-2 and ERA-Interim with annual and summer differences around 40%, respectively. This suggests that, in terms of grid percentages corresponding to underestimated and overestimated precipitation LTs, the products' performance varies at daytime and nighttime.

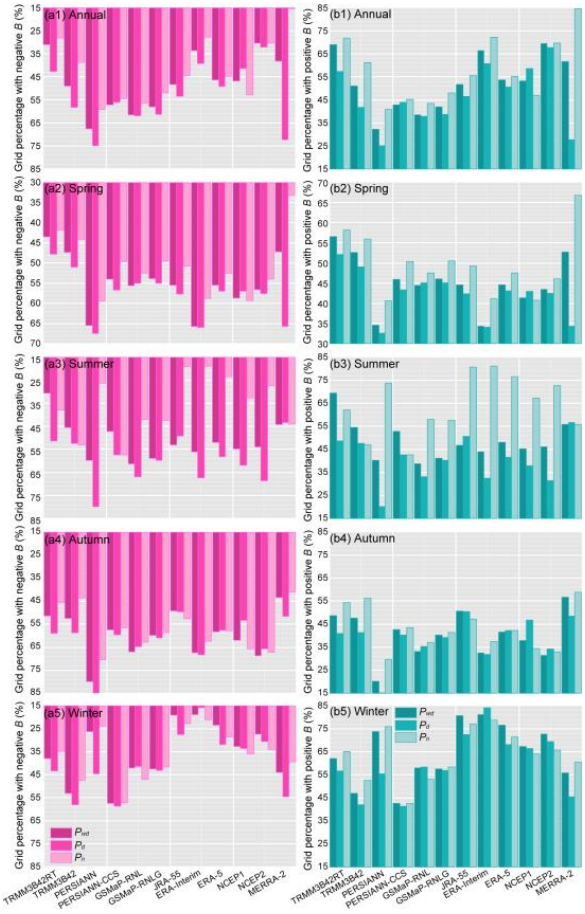

Figure 4. Grid percentages with negative (**a1**–**a5**) and positive biases (Bs; **b1**–**b5**) for annual and seasonal LTs across MC.

Taking MC as a whole, regional mean Bs for LT_{wd}, LT_d and LT_n derived from each product were calculated and are shown in Figure 5(a1–a5). At the annual scale, five products exhibited positive Bs for LT_{wd}, with a range from 0.39 mm/yr for TRMM3B42 to 10.10 mm/yr for NCEP2, while four products exhibited positive Bs for LT_d, ranging from 1.44 mm/yr for TRMM3B42RT to 5.01 mm/yr for NCEP2. Negative Bs were found for the remaining products, of which the lowest values of –7.88 mm/yr and –4.98mm/yr for LT_{wd} and LT_d, respectively, were recorded for PERSIANN (Figure 5(a1)). In contrast, seven products overestimated annual LT_n, particularly ERA-Interim, NCEP2, and MERR-2 with Bs > 5 mm/yr, while the other products' Bs were all negative and generally <−3 mm/yr. Regarding the spring LTs (Figure 5(a2)), TRMM3B42RT, TRMM3B42, and MERRA-2 had positive Bs < 1.40 mm/yr, except for LT_d. However, negative spring Bs were found in the remaining products, ranging from −2.60 mm/yr (−1.61 mm/yr) for JRA-55 to −0.88 mm/yr (−0.51 mm/yr) for ERA-Interim for LT_{wd} (LT_d), and from −1.52 mm/yr for NCEP1 to −0.31 mm/yr for PERSIANN-CCS for LT_n. For summer LT_{wd} and LT_n (Figure 5(a3)), most of the products exhibited positive Bs, while LT_d was generally underestimated by the products (excluding TRMM3B42RT and NCEP1). Despite that, summer Bs for LTs were generally from −2 mm/yr to 2 mm/yr, except for TRMM3B42RT LT_{wd} and LT_n, and MERRA-2 LT_n with Bs >

2 mm/yr, and PERSIANN-CCS LT_{wd} and LT_d with Bs < −2 mm/yr. In autumn (Figure 5(a4)), absolute values of Bs for LTs from TRMM3B42, TRMM3B42RT, and MERRA-2 were all < 0.60 mm/yr, but Bs were generally < −1 mm/yr for the remaining products, and even some were lower than −4 mm/yr (i.e., PERSIANN, and NCEP2 for LT_{wd}). In contrast, the majority of products overestimated winter LT_{wd}, LT_d, and LT_n, and Bs were generally < 3 mm/yr, with exceptions of JRA-55, ERA-Interim, and ERA-5 having Bs > 3 mm/yr (Figure 5(a5)). In terms of Bs for annual LT_d and LT_n (Figure 5(a1)), there were differences for some products, i.e., TRMM3B42RT, PERSIANN-CCS, and ERA-Interim with large differences > 2 mm/yr, and TRMM3B42, JRA-55, ERA-5, NCEP1, and MERRA-2 showing different sign (positive/negative). Evident differences in Bs existed for some products in each season (Figure 3(a2–a5)); in summer there were eight products with different signs of Bs and four products with large differences (around ±1 mm/yr) but the same sign.

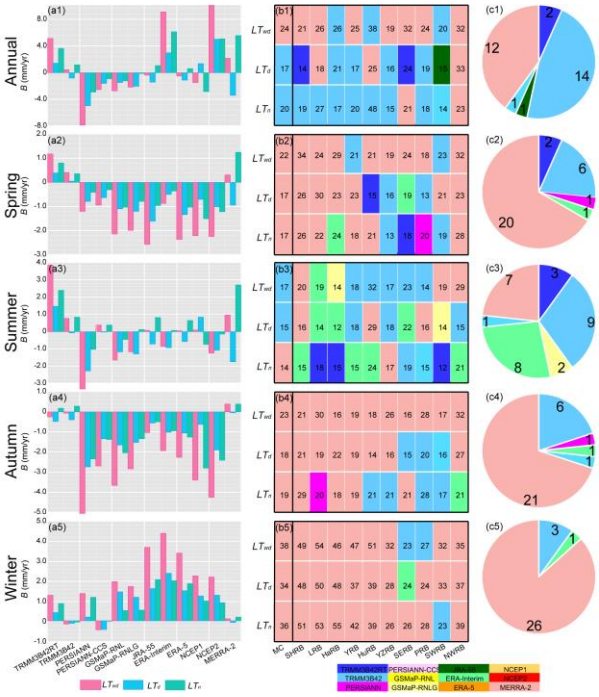

Figure 5. MC Bs derived from the selected 12 precipitation products (**a1**–**a5**), B-based optimal products (OPs) for MC and ten WRRs (**b1**–**b5**), and number of cases corresponding to B-based OPs on an annual or seasonal scale for ten WRRs (**c1**–**c5**). In figures (**b1**–**b5**), the number of each box represents grid percentage (%) of OP, which has been labelled with different colors. The number of figures (**c1**–**c5**) indicates the amount of a certain OP.

Considering offset effects of positive and negative Bs within MC and each WRR, we calculated the percentage of grids with the minimum absolute B for each product, and B-based OPs were identified as the product with the largest grid percentage (Figure 5(b1–b5,c1–c5)). Except for annual LT_d and LT_n and summer LT_{wd} and LT_d, for which the OP was TRMM3B42, the OP for all other LTs was MERRA-2 for MC (Figure 5(b1–b5)). For annual cases of the ten WRRs (Figure 5(c1)), the OPs were TRMM3B42 and MERRA-2 in 14 and 12 cases, respectively. Furthermore, the OP for most WRRs was MERRA-2 for annual LT_{wd}, and TRMM3B42 for both annual LT_d and LT_n (Figure 5(b1)). For B-based OPs of spring and autumn LT_{wd} (Figure 5(b2,b4)), the OP was MERRA-2 in most WRRs, while the OPs for LT_d and LT_n in southern and northern WRRs differed and were mainly TRMM3B42RT and MERRA-2, respectively. In summer (Figure 5(b3)), there were differences in OP for the three LTs, i.e., most WRRs with OPs of TRMM3B42 and MERRA-2 for LT_{wd}, TRMM3B42, MERRA-2, and ERA-Interim for LT_d, and ERA-Interim and TRMM3B42RT for LT_n. During winter (Figure 5(b5)), with four exceptions, all cases had an OP of MERRA-2. Overall, more than 20 cases had MERRA-2 as their OP for spring,

autumn, and winter, while TRMM3B42 had fewer than six cases. For summer, the OP was TRMM3B42 for nine cases, ERA-Interim for eight cases, and MERRA-2 for seven cases (Figure 5(c2–c5)).

3.4. Evaluation Using Error Metric

The MC RMSEs for LT_{wd}, LT_d and LT_n of each product are illustrated in Figure 6(a1–a5). For MC, TRMM3B42, TRMM3B42RT, PERSIANN, PERSIANN-CCS, and MERRA-2, RMSEs for annual LT_{wd}, LT_d and LT_n were lowest (<20.00 mm/yr for LT_{wd}; <10.00 mm/yr for LT_d and LT_n); this indicates that the accuracy of the five products, especially TRMM3B42, in detecting annual LTs is better. Except for PERSIANN-CCS and MERRA-2, the slightly smaller differences in annual RMSE for LT_d and LT_n from the remaining products suggests a comparable accuracy at daytime and nighttime. For LT_{wd}, LT_d, and LT_n, the largest RMSEs for each product occurred in summer and the smallest occurred in winter, due to their larger and smaller portion of annual MC precipitation, respectively. In each season, the minimum RMSE of the three LTs generally came from TRMM3B42 and MERRA-2, however, larger RMSEs were frequently found for GSMaP-RNL, GSMaP-RNLG, JRA-55, ERA-5, NCEP1, and NCEP2. Comparing RMSEs of LT_d and LT_n for each product in each season, LT_d for most of the products exhibited larger and smaller values in summer and the other three seasons, respectively; it should be noted that differences between LT_d and LT_n were not evident, excluding PERSIANN-CCS, which had an absolute difference > 2 mm/yr in winter.

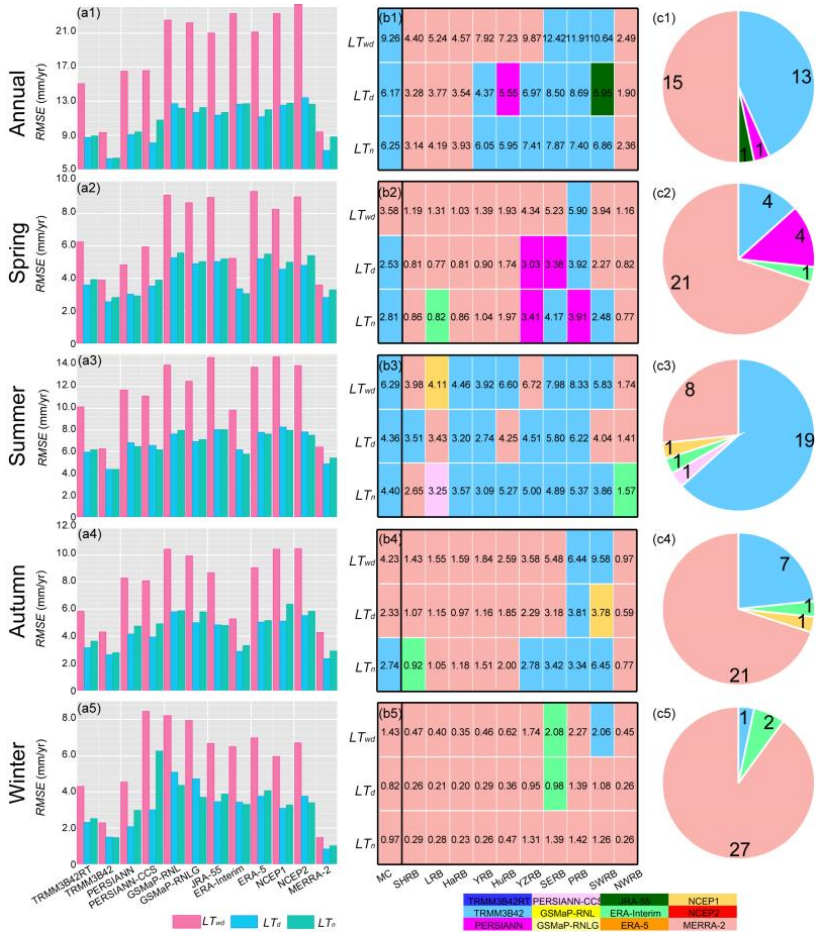

Figure 6. MC root mean square error (RMSE) derived from the selected 12 precipitation products (**a1**–**a5**), RMSE-based optimal products (OPs) for MC and ten WRRs (**b1**–**b5**), and number of cases corresponding to RMSE-based OPs for annual or seasonal scale in ten WRRs (**c1**–**c5**). In figures (**b1**–**b5**), the number of each box represents RMSEs (mm/yr) of OP, which are labelled with different colors. The number of figures (**c1**–**c5**) indicates the amount of a certain OP.

Figure 6(b1–b5) illustrate the RMSE-based OPs of LTs for MC and WRRs. In general, the MC RMSE-based Ops for the three LTs for annual, spring (excluding LT_{wd}) and summer were TRMM3B42, while MERRA-2 was the autumn OP (excluding LT_n) and winter OP. At the annual scale, 13 cases had an RMSE-based OP of TRMM3B42, generally in southern WRRs, YRB, and HuRB; the remaining four WRRs had MERRA-2 as their OP (Figure 6(b1,c1)). In spring, the RMSE-based OP for the three LTs in northern WRRs and LT_{wd} in southern WRRs was MERRA-2, corresponding to 21 cases; eight cases had TRMM3B42 and PERSIANN as their OP, and these mainly appeared in LT_d and LT_n of southern WRRs (Figure 6(b2,c2)). During summer (Figure 6(b3,c3)), with three exceptions, all cases had TRMM3B42 (19 cases) and MERRA-2 (eight cases) as their OPs. In autumn, TRMM3B42 was the OP in seven cases mainly in southern WRRs (except for LT_{wd} and LT_d in YZRB and SERB), followed by MERRA-2, which was the OP in 21 cases (Figure 6(b4,c4)). With the exceptions of LT_{wd} and LT_d in YZRB and LT_{wd} in SWRB, MERRA-2 was the OP in 27 cases in winter (Figure 6(b5,c5).

3.5. Evaluation Using Metric of Sign Accuracy

To examine the degree of agreement between the positive or negative sign of LTs from the products and the observed values, metrics of AS and JAS were computed over MC and are illustrated in Figure 7(a1–a5) and Figure 8(a1–a5), respectively. At the annual scale, MC AS values for LT_{wd}, LT_d, and LT_n from all products were > 50%. This suggests that the observed signs of LTs can be captured by the products, among which TRMM3B42RT, TRMM3B42, and MERRA-2 showed AS values > 70% for the three LTs, followed by PERSIANN, PERSIANN-CCS, ERA-Interim, and NCEP2 with values > 60% (Figure 7(a1)). During each season (Figure 7(a2–a5)), TRMM3B42RT, TRMM3B42, PERSIANN, PERSIANN-CCS, ERA-Interim, and MERRA-2 showed MC AS values > 60% for the three LTs, and the largest percentage (>70%) was found for TRMM3B42RT (except in winter), TRMM3B42 (except in winter), and MERRA-2. For the remaining six products, their AS-based performances differed among seasons. For example, all of them corresponded to autumn AS values > 50% for the three LTs; however, the values in the other seasons were generally < 50%. As shown in Figure 7(b1–b5), MC annual and summer AS-based OPs were MERRA-2 for LT_{wd}, but TRMM3B42 for LT_d and LT_n. For MC LTs in the remaining three seasons, the AS-based OP was MERRA-2, except for spring LT_d. Of the 30 annual cases in ten WRRs, AS-based OPs were MERRA-2 in 13 cases, TRMM3B42 in six cases and TRMM3B42RT in three cases, and there was more than one OP in five cases (Figure 7(b1–c1)). Among the ten WRRs, there were five or more OPs for each of the three LTs, indicating obvious regional differences for the products in detecting the same signs of LTs. In spring (Figure 7(b2–c2)), the AS-based OPs were MERRA-2 (15 cases), TRMM3B42 (five cases), TRMM3B42RT (four cases), ERA-Interim (four cases), and PERSIANN (two cases). Southern WRRs generally had OPs of TRMM3B42, TRMM3B42RT, and PERSIANN, while the OPs for northern WRRs were MERRA-2 and ERA-Interim. During summer (Figure 7(b3–c3)), AS-based OP was TRMM3B42 in 14 cases, mainly in southern WRRs, HaRB, YRB, and HuRB; and the OP was MERRA-2 in nine cases primarily in SHRB, LRB and NWRB. Of the 30 cases in autumn (Figure 7(b4–c4)), MERRA-2 was identified as the AS-based OP in 14 cases mainly in northern WRRs (excluding YRB), however, in eight cases the OP was TRMM3B42 generally in YRB, YZRB, and SWRB. Each of the six autumn cases in SERB and PRB had more than one OP. Regarding the 30 cases in winter (Figure 7(b5–c5)), 26 cases had AS-based OPs of MERRA-2 (22 cases) and TRMM3B42RT (four cases).

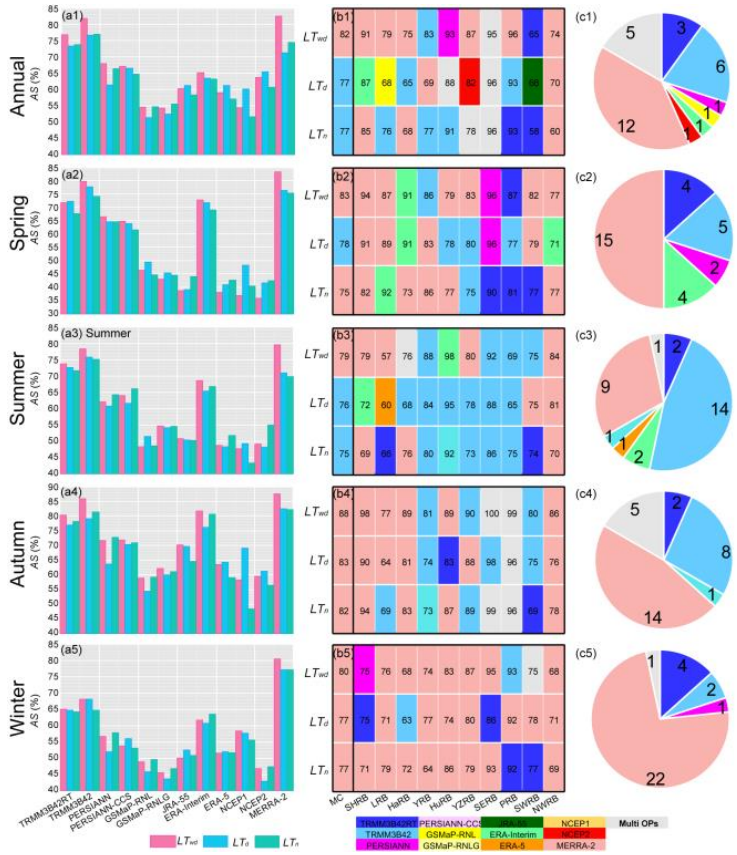

Figure 7. MC accurate sign (AS) values derived from the selected 12 precipitation products (**a1**–**a5**), AS-based optimal products (OPs) for MC and ten WRRs (**b1**–**b5**), and the number of cases corresponding to AS-based OPs (**c1**–**c5**) for the annual or seasonal scales in ten WRRs. For figures (**a1**–**a5**), AS is computed with Equation (5), indicating the degree of agreement between the positive or negative sign of precipitation trends from the products and the observed data. In figures (**b1**–**b5**), the number in each box represents AS values (%) of the OP, which have been labelled with different colors. The number of figures (**c1**–**c5**) indicates the amount of a certain OP.

Except for TRMM3B42RT, TRMM3B42, and MERRA-2 with annual JAS values > 55% (Figure 8(a1)), values of this metric were all below 50%, suggesting that these products have limited capacity to detect the co-variations of daytime and nighttime precipitation, in spite of relatively large AS for LTs (Figure 7(a1)). In spring (Figure 8(a2)), the best JAS-based performance was found in TRMM3B42 and MERRA-2 (with JAS around 60%), followed by TRMM3B42RT and ERA-Interim. Excluding PERSIANN and PERSIANN-CCS, the other six products had spring JAS values < 25%. JRA-55 and ERA-5 had JAS < 20%, which indicated that those six products could not capture the co-variations of spring precipitation changes at daytime and nighttime. During summer (Figure 8(a3)), TRMM3B42RT, TRMM3B42, and MERRA-2 performed the best (with JAS values > 53%), followed by PERSIANN, PERSIANN-CCS, and ERA-Interim with the next best performance (with JAS around 45%), and the remaining products (with JAS around 30%). For autumn (Figure 8(a4)), seven of the products correctly detected the co-variations of daytime and nighttime precipitation changes in >50% grids (i.e., JAS > 50%), particularly for TRMM3B42RT, TRMM3B42, ERA-Interim, and MERRA-2, which had JAS values > 64%. GSMaP-RNL and NCEP1 had JAS values near to 40% and performed the worst. Regarding winter JAS (Figure 8(a5)), values > 50% only appeared for MERRA-2, and the minima (around 25%) were found in GSMaP-RNL, GSMaP-RNLG, and NCEP2. As depicted in Figure 8b, MC annual and summer JAS-based OP was TRMM3B42, but for the other seasons the OP was MERRA-2. Except for SHRB and NWRB, with MERRA-2 as their annual JAS-based OP, the remaining WRRs generally had TRMM3B42 as the OP (Figure 8b). In southern WRRs, most had OPs of TRMM3B42 and

PERSIANN in spring and summer but MERRA-2 and PERSIANN in autumn and winter. By contrast, summer JAS-based OPs were MERRA-2 and TRMM3B42 in northern WRRs, while MERRA-2 was the OP in most northern WRRs.

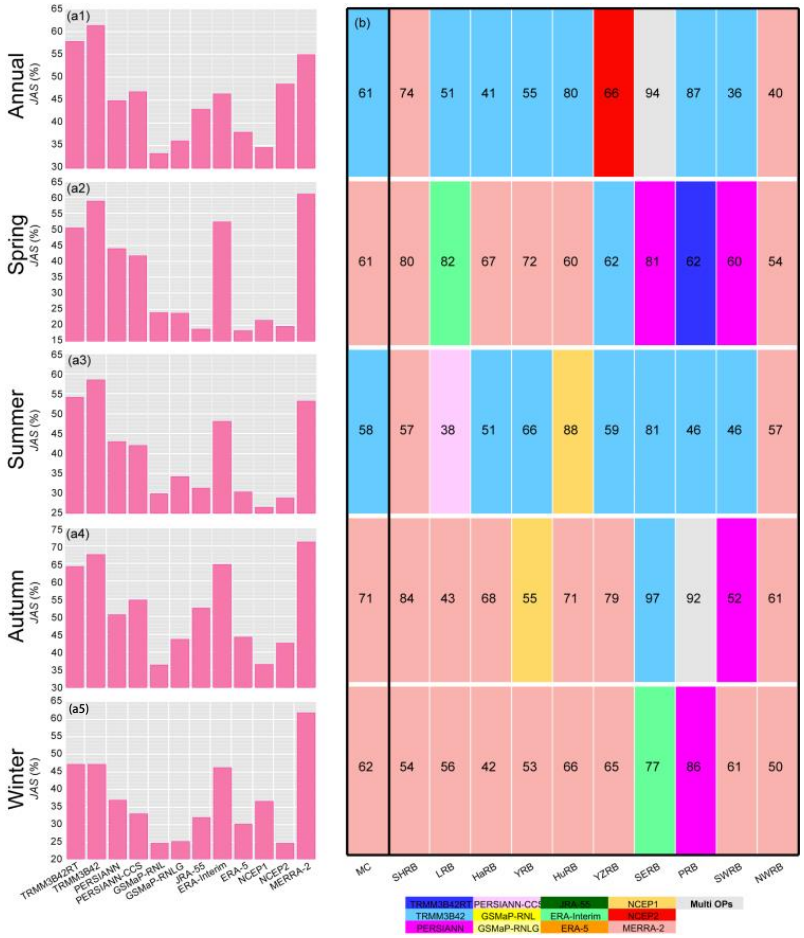

Figure 8. MC joint AS (JAS) values derived from the selected 12 precipitation products (**a1**–**a5**), and JAS-based optimal products (OPs) for MC and ten WRRs (**b**). For figures (**a1**–**a5**), JAS is computed with Equation (6), indicating the capacity of a given product to rightly detect the signs of both P_d and P_n changes relative to the observed data. In (**b**), the number in each box represents JAS values (%) of the OP, which has been labelled with different colors.

4. Discussion

4.1. Possible Causes for Variation in Performance among Precipitation Products

In this study, we explored the reliability of the satellite-based and reanalysis products in capturing precipitation linear trends across MC, and found that the performances of these products exhibited clear differences. In general, TRMM3B42 and MERRA-2 showed the best overall performance. There are several possible explanations for the performance variation, e.g., input data, onboard sensors, and retrieval algorithm for the satellite-based products; and numerical models and their structures, parameterizations (especially for schemes about precipitation processes), and assimilation systems for the reanalysis products. Nonetheless, quantitatively identifying the impacts of these factors is difficult and beyond the scope of this study. As a result, we would like to discuss the potential causes of different performance among the precipitation products with the same retrieval algorithm or model structures, i.e., TRMM3B42RT vs. TRMM3B42, PERSIANN vs. PERSIANN-CCS, GSMaP-RNL vs. GSMaP-RNLG, ERA-Interim vs. ERA-5, and NCEP1 vs. NCEP2. It is evident that TRMM3B42 generally outperforms TRMM3B42RT, could be attributed to the fact that the former incorporates rain gauge data (i.e., monthly

GPCP and CAMS data; [32]) to adjust the precipitation estimates. In some WRRs, TRMM3B42RT performed better or was the OP, implying that the TRMM3B42 precipitation trends were occasionally overcorrected due to an inappropriate correction method (e.g., daily TRMM3B42RT adjusted with monthly observation; [32]). For PERSIANN and PERSIANN-CCS, their major differences are that the latter includes a cloud classification system based on cloud height, areal extent, and variability of texture estimated from satellite imagery to more accurately describe the relationship between precipitation rate and brightness temperature [35]. Despite that, the performance of PERSIANN in detecting precipitation trends was better than PERSIANN-CCS across MC based on most of the validation metrics. This indicates that the cloud classification system within PERSIANN-CCS has limited effectiveness in improving the estimated precipitation trends, although PERSIANN-CCS has been found to outperform PERSIANN in estimating precipitation amount over some regions of MC and its sub-regions (e.g., Tibetan Plateau and Yangtze River Basin, [88–91]). For the bias metric, PERSIANN-CCS performed better, mainly because, within a given region, the functions between precipitation rate and brightness temperature are established for each categorization of cloud-patch, and thus the regional biases are more likely to be offset. Relative to other satellite-based products, the two GSMaP products had the worst performance in MC and ten WRRs, indicating that the algorithm employed by GSMaP-RNL and GSMaP-RNLG may be problematic in capturing precipitation trends. Meanwhile, some studies also found that the GSMaP products had very low performance in capturing precipitation magnitudes and hydrological modeling over MC [92] and some Asian regions, such as the VuGia–ThuBon River Basin of Vietnam [93], and Mekong River Basin [94]. Moreover, the worst performance of GSMaP-RNLG in terms of specific validation metric suggests that its gauge-based correction processes are not efficient to adjust the precipitation trend. Relative to ERA-Interim, ERA-5 had a more advanced assimilation system and more and newer observational inputs, and thus was observed to have better performances (e.g., lower bias and root-mean squared error, and higher correlation coefficient) to reproduce precipitation in some regions, [45,91,95]. However, we found that in the study the ERA-5 precipitation trends poorly match the observations relative to the ERA-Interim. These findings are consistent with the findings of Nogueira across the globe [96], who pointed out that the trend of global-mean rainfall in ERA-Interim was closer to GPCP than ERA-5, and suggested that the possible causes were associated with the global energy budget [97,98]. Due to NCEP2 with new system components including simple precipitation assimilation over land surfaces for improved soil wetness [43], NCEP2 precipitation agreed more closely with gauge measurements than NCEP1 data in China [99], USA [100], and Central Equatorial Africa [101]; by contrast, comparisons between NCEP1 and NCEP2 in representing precipitation linear trends show that no obvious differences existed. This may be related to significant time-varying jumps in the late 2000s within NCEP2, mainly due to the changes in observing systems, such as the introduction of new data into the assimilation systems [102,103]; this is also the possible cause of poor performance for JRA-55 [101]. The validation metrics clearly show that, based on precipitation linear trends, MERRA-2 performed better than other reanalysis products and even satellite-based precipitation products in MC. The better performances of MEERA-2 for representing precipitation amount were also found in other regions (e.g., Nepal, and the Pamir region of Tajikistan, [104,105]). Some scholars pointed that the possible causes are related to the advanced data assimilation technique within MERRA-2 and the bias corrections of MERRA-2 precipitation [45]. We should note that for a given product there are differences in performance of detecting precipitation trends within a day (e.g., daytime and nighttime annual correlation coefficients for ERA-Interim) and among seasons (e.g., smaller winter correlation coefficient values for PERSIANN but larger values in the other three seasons), mainly due to the different physical mechanisms controlling precipitation processes [69–71,73,74]. For example, some studies stated that sea–land breeze is closely associated with the diurnal cycle of precipitation in coastal areas, while topography and mountain–valley breeze plays an important role in the interior [73,74]. Therefore, to increase the accuracy of sub-daily and seasonal precipitation estimates, specific algorithms for the satellite-based products and specific model structures for the reanalysis products should be developed.

4.2. Uncertainties from Rain Gauge Data

We employed rain gauge data as a reference to validate the 12 precipitation products in detecting precipitation trends at different time scales across MC. It should be noted that the inherent uncertainties within the gauge data, which are related to flaws in calibration, wind-related under-catch, and wetting and evaporation losses, could bias the gauge measurements from the real values and weaken the robustness of the validation results (e.g., [106–109]). For example, Shedekar et al. [109] found that relative to the actual rainfall depths, the precipitation measurements from three calibrated tipping-bucket rain gauges were underestimations, particularly for heavy rainfall, and they highlighted that the biases were closely associated with the gauge calibrations. When it is windy, gauge observations are often impacted by wind-related under-catch effects through deflecting the flow and inducing eddies and turbulence around the gauges [108–111]. In general, wind can cause some raindrops, especially smaller ones, to miss the funnel or fall at an inclination, and finally impact the catch efficiency of the gauges. To what extent wind influences the accuracy of the gauge measurements is dependent on ambient wind speed, raindrop size distribution, and gauge design [110]. Sieck et al. [110] reported that, compared to rainfall from collocated buried gauges, wind-exposed aboveground gauges would likely observe about 2–10% less precipitation. Due to water adhering to the inside walls of the gauge and then evaporating, the gauge-recorded precipitation is generally lower than the true value, and the biases vary among gauge configurations (e.g., frequency of emptying) and precipitation types [106,112,113]. A Russian study revealed that, for each record of rainfall measurement, the mean average wetting loss was 0.2 mm, but for both snow and mixed precipitation the value was 0.15 mm [112]. Due to being exposed to the atmosphere, water within rain gauges is usually evaporated (i.e., evaporation losses; [114–117]). It is reported that evaporation losses for gauged precipitation generally range from 0.1 to 0.8 mm/day or from 0 to 1%; however, the magnitudes differ among gauge types, climate backgrounds, and seasons [114]. The combined effects induced by the aforementioned factors on rain gauge measurements are likely to underestimate the recorded precipitation [118], e.g., the bias-corrected annual precipitation (removing the uncertainties within raw observations) being 30–330 mm or 10–65% higher than the raw observations over Siberia.

Usually, the quality of precipitation observations is accompanied by an issue of standardization, or lack of, which is mainly due to changes in gauge instruments, station relocation and environment, etc. [119–122]. Moreover, these factors result in negative impacts on data quality, in particular for climate researches using long-term time series (e.g., linear trend evaluation in this study). Before using the gauged precipitation measurements, it is necessary to reduce and even remove the associated uncertainties, e.g., adjust the raw records using metadata about gauges, and at least eliminating sites with non-homogeneous measurements identified by some statistic methods. The Pettitt test has been used to remove sites with non-homogenous measurements due to a lack of metadata for the selected sites, but there is no guarantee that the remaining sites have no issues, which can weaken the confidence level of the results. Besides, mismatches between representatives of gauge precipitation (i.e., a point of space in time accumulation) and selected products (i.e., a snapshot of time in space aggregation) are likely to have an effect on the accuracy and precision of qualitative and quantitative assessments of various precipitation products [123–125]. For instance, the spatial resolution of all the 12 products is generally lower than $0.25^\circ \times 0.25^\circ$ (except for PERSIANN-CCS), across which the estimated precipitation was averaged, while the spatial representation of a gauge is much smaller than the coverage of the pixel of the 12 products. Considering the variability of precipitation over a small spatial extent, a sparse gauge network may not identify meso-/micro-scale weather system-associated precipitation (e.g., convective precipitation; [126–129]); thus, gauge precipitation measurements may be smaller in magnitude and frequency than the ground-truthed values for a given pixel.

5. Conclusions

As important surrogate for precipitation estimates, various satellite-based and reanalysis precipitation products need to be validated from different perspectives. Especially, the information

about the capacity of the satellite-based and reanalysis precipitation is scarce on a sub-daily scale, especially for China. However, the assessments regarding precipitation trends are fundamental for selecting the reliable products to explore precipitation changes, particularly for regions with limited or even no observations. Thus, with a motivation to explore twelve popular precipitation products (i.e., six satellite-based and six reanalysis products) in detecting precipitation linear trends across MC, we collected daytime and nighttime observations from a dense rain gauge network during 2003–2017, and examined LT_{wd}, LT_d, and LT_n across mainland China. We found that annual and seasonal LT_{wd}, LT_d, and LT_n for MC and most WRRs were positive but with regional differences. In terms of magnitude and sign (i.e., decreasing and increasing), LT_d and LT_n in a certain region showed evident differences, confirming the necessity to evaluate precipitation products at a sub-daily scale. Then, several statistical metrics (i.e., CC, B, RMSE, AS, and JAS) were employed to identify the differences and agreements of LTs for MC and ten WRRs between twelve precipitation products and gauge observations on sub-daily scale. In general, values of a given metric for annual and seasonal LT_{wd}, LT_d, or LT_n differed among products. Meanwhile, performances for single product varied among seasons and between daytime and nighttime. At last, the metric-based OPs were identified for MC and each WRR. The metric-based OPs varied among regions and seasons, and between daytime and nighttime, but the most frequent OPs were TRMM3B42, ERA-Interim, and MERRA-2.

The comparison of satellite-based and reanalysis products in ability to detect precipitation linear trends in this study provides suggestions for developers and the potential users of these products across mainland China. For a given product, varying performance for different validation metrics at different timescales (between daytime and nighttime) suggests that the product's group can try to develop specific algorithms/models during a certain season (at a sub-daily scale) and correction procedures to improve its capacity to reproduce precipitation trends. For the potential users who focus on long-term precipitation changes across MC, this study provides necessary and detailed information about the existing popular precipitation products' performances in detecting linear trends, which is fundamental to obtaining robust conclusions.

Author Contributions: Conceptualization, S.S. and W.S.; methodology, W.S. and H.C.; software, S.Z.; validation, S.S., W.S. and Y.Z.; formal analysis, S.S., R.C. and W.S.; investigation, S.S.; resources, S.S. and H.S.; data curation, W.S. and R.C.; writing—original draft preparation, S.S., W.S. and S.Z.; writing—review and editing, S.S., G.W. and H.C.; visualization, S.S and W.S.; supervision, S.S., G.W. and H.C.; project administration, S.S., G.W. and H.C.; funding acquisition, S.S., G.W. and H.C. All authors discussed the results and revised the manuscript. All authors have read and agreed to the published version of the manuscript.

Funding: This work was jointly supported by the National Key Research and Development Program of China (Grant No. 2018YFC1507101), Natural Science Foundation of China (Grant Nos. 41875094), and Qinglan Project of Jiangsu Province of China.

Acknowledgments: We thank all data (i.e., satellite-based and reanalysis precipitation products) developers, and their managers and funding agencies, whose work and support were essential for obtaining the datasets, without which the analyses conducted in this study would have been impossible. Notably, precipitation data at more than 2000 gauges are not available to the public, but they can be obtained and used through cooperation with the CMA. Source code used to conduct this study is available from the authors upon request (sun.s@nuist.edu.cn or ppsunsanlei@126.com).

Conflicts of Interest: The authors declare no conflict of interest.

References

1. Cui, Y.; Yan, D.; Hong, T.; Xiao, C.; Luo, X.; Zhang, Q. Comparison of typical year and multiyear building simulations using a 55-year actual weather data set from China. *Appl. Energy* **2017**, *195*, 890–904. [CrossRef]
2. Kidd, C.; Becker, A.; Huffman, G.J.; Muller, C.L.; Joe, P.; Skofronick-Jackson, G.; Kirschbaum, D.B. So How much of the Earth's surface is covered by rain gauges? *Bull. Am. Meteorol. Soc.* **2017**, *98*, 69–78. [CrossRef] [PubMed]
3. Zhou, C.; Wang, K. Contrasting daytime and nighttime precipitation variability between observations and eight reanalysis products from 1979 to 2014 in China. *J. Clim.* **2017**, *30*, 6443–6464. [CrossRef]

4. Milly, P.C.D.; Dunne, K.A.; Vecchia, A.V. Global patterns of trends in streamflow and water availability in a changing climate. *Nature* **2005**, *438*, 347–350. [CrossRef] [PubMed]
5. Sorooshian, S.; AghaKouchak, A.; Arkin, P.; Eylander, J.; Foufoula-Georgiou, E.; Harmon, R.; Hendrickx, J.M.H.; Imam, B.; Kuligowski, R.; Skahill, B.; et al. Advanced concepts on remote sensing of precipitation at multiple scales. *Bull. Am. Meteorol. Soc.* **2011**, *92*, 1353–1357. [CrossRef]
6. Sun, S.; Zhou, S.; Shen, H.; Chai, R.; Chen, H.; Liu, Y.; Shi, W.; Wang, J.; Wang, G.; Zhou, Y. Dissecting Performances of PERSIANN-CDR Precipitation Product over Huai River Basin, China. *Remote Sens.* **2019**, *11*, 1805. [CrossRef]
7. Thornes, J.; Bloss, W.; Bouzarovski, S.; Cai, X.; Chapman, L.; Clark, J.; Dessai, S.; Du, S.; van der Horst, D.; Kendall, M.; et al. Communicating the value of atmospheric services. *Meteorol. Appl.* **2010**, *17*, 243–350. [CrossRef]
8. Murthy, C.S.; Singh, J.; Kumar, P.; Sai, M.V.R.S. A composite index for drought hazard assessment using CPC rainfall time series data. *Int. J. Environ. Sci. Technol.* **2017**, *14*, 1981–1988. [CrossRef]
9. Sun, S.; Chen, H.; Ju, W.; Wang, G.; Sun, G.; Huang, J.; Ma, H.; Gao, C.; Hua, W.; Yan, G. On the coupling between precipitation and potential evapotranspiration: Contributions to decadal drought anomalies in the Southwest China. *Clim. Dyn.* **2017**, *48*, 3779–3797. [CrossRef]
10. Sun, S.; Li, Q.; Li, J.; Wang, G.; Zhou, S.; Chai, R.; Hua, W.; Deng, P.; Wang, J.; Lou, W. Revisiting the evolution of the 2009–2011 meteorological drought over Southwest China. *J. Hydrol.* **2019**, *568*, 385–402. [CrossRef]
11. Wei, J.; Jin, Q.; Yang, Z.-L.; Dirmeyer, P.A. Role of ocean evaporation in California droughts and floods. *Geophys. Res. Lett.* **2016**, *43*, 6554–6562. [CrossRef]
12. Berghuijs, W.R.; Aalbers, E.E.; Larsen, J.R.; Trancoso, R.; Woods, R.A. Recent changes in extreme floods across multiple continents. *Environ. Res. Lett.* **2017**, *12*. [CrossRef]
13. Hong, Y.; Gochis, D.; Cheng, J.T.; Hsu, K.L.; Sorooshian, S. Evaluation of PERSIANN-CCS rainfall measurement using the name event rain gauge network. *J. Hydrometeorol.* **2007**, *8*, 469–482. [CrossRef]
14. Nguyen, P.; Ombadi, M.; Sorooshian, S.; Hsu, K.; AghaKouchak, A.; Braithwaite, D.; Ashouri, H.; Thorstensen, A.R. The PERSIANN family of global satellite precipitation data: A review and evaluation of products. *Hydrol. Earth Syst. Sci.* **2018**, *22*, 5801–5816. [CrossRef]
15. Pan, M.; Li, H.; Wood, E.F. Assessing the skill of satellite-based precipitation estimates in hydrologic applications. *Water Resour. Res.* **2010**, *46*, W09535. [CrossRef]
16. Xie, P.; Janowiak, J.E.; Arkin, P.A.; Adler, R.; Gruber, A.; Ferraro, R.; Huffman, G.J.; Curtis, S. GPCP pentad precipitation analyses: An experimental dataset based on gauge observations and satellite estimates. *J. Clim.* **2003**, *16*, 2197–2214. [CrossRef]
17. Kidd, C.; Kniveton, D.R.; Todd, M.C.; Bellerby, T.J. Satellite rainfall estimation using combined passive microwave and infrared algorithms. *J. Hydrometeorol.* **2003**, *4*, 1088–1104. [CrossRef]
18. Wentz, F.J.; Ricciardulli, L.; Hilburn, K.; Mears, C. How much more rain will global warming bring? *Science* **2007**, *317*, 233–235. [CrossRef]
19. Ebert, E.E.; Manton, M.J.; Arkin, P.A.; Allam, R.J.; Holpin, C.E.; Gruber, A. Results from the GPCP Algorithm Intercomparison Programme. *Bull. Am. Meteorol. Soc.* **1996**, *77*, 2875–2887. [CrossRef]
20. Sapiano, M.R.P.; Arkin, P.A. An intercomparison and validation of high-resolution satellite precipitation estimates with 3-hourly gauge data. *J. Hydrometeorol.* **2009**, *10*, 149–166. [CrossRef]
21. Gou, Y.; Ma, Y.; Chen, H.; Weng, Y. Radar-derived quantitative precipitation estimation in complex terrain over the eastern Tibetan Plateau. *Atmos. Res.* **2018**, *203*, 286–297. [CrossRef]
22. Maddox, R.A.; Zhang, J.; Gourley, J.J.; Howard, K.W. Weather radar coverage over the contiguous United States. *Weather Forecast.* **2002**, *17*, 927–934. [CrossRef]
23. Turk, F.J.; Haddad, Z.S.; Kirstetter, P.; You, Y.; Ringerud, S. An observationally based method for stratifying a priori passive microwave observations in a Bayesian-based precipitation retrieval framework. *Q. J. R. Meteorol. Soc.* **2018**, *144*, 145–164. [CrossRef]
24. Kuligowski, R.J.; Li, Y.; Zhang, Y. Impact of TRMM data on a low-latency, high-resolution precipitation algorithm for flash-flood forecasting. *J. Appl. Meteorol. Climatol.* **2013**, *52*, 1379–1393. [CrossRef]
25. Ashouri, H.; Hsu, K.; Sorooshian, S.; Braithwaite, D.K.; Knapp, K.R.; Cecil, L.D.; Nelson, B.R.; Prat, O.P. PERSIANNCDR: Daily precipitation climate data record from multi-satellite observations for hydrological and climate studies. *Bull. Am. Meteorol. Soc.* **2015**, *96*, 69–83. [CrossRef]

26. Adler, R.F.; Huffman, G.J.; Chang, A.; Ferraro, R.; Xie, P.P.; Janowiak, J.; Rudolf, B.; Scjneider, U.; Curtis, S.; Gruber, D.B.A.; et al. The version-2 global precipitation climatology project (GPCP) monthly precipitation analysis (1979–present). *J. Hydrometeorol.* **2003**, *4*, 1147–1167. [CrossRef]
27. Gebregiorgis, A.; Hossain, F. How much can a priori hydrologic model predictability help in optimal merging of satellite precipitation products? *J. Hydrometeorol.* **2011**, *12*, 1287–1298. [CrossRef]
28. Michaelides, S.; Levizzani, V.; Anagnostou, E.; Bauer, P.; Kasparis, T.; Lane, J.E. Precipitation: Measurement, Remote Sensing, Climatology and Modeling. *Atmos. Res.* **2009**, *94*, 512–533. [CrossRef]
29. Prigent, C. Precipitation retrieval from space: An overview. *Comptes Rendus Geosci.* **2010**, *342*, 380–389. [CrossRef]
30. Screen, J.A.; Simmonds, I. Erroneous arctic temperature trends in the ERA-40 reanalysis: A closer look. *J. Clim.* **2011**, *24*, 2620–2627. [CrossRef]
31. Turk, J.T.; Mostovoy, G.V.; Anantharaj, V. The NRL-Blend High Resolution Precipitation Product and its Application to Land Surface Hydrology. In *Satellite Rainfall Applications for Surface Hydrology*; Gebremichael, M., Hossain, F., Eds.; Springer: Dordrecht, The Netherlands, 2010.
32. Huffman, G.J.; Adler, R.F.; Bolvin, D.T.; Gu, G.; Nelkin, E.J.; Bowman, K.P.; Yong, Y.; Stocker, E.F.; Wolff, D.B. The TRMM Multi-satellite Precipitation Analysis (TMPA): Quasi-global, multi-year, combined-sensor precipitation at fine scales. *J. Hydrometeorol.* **2007**, *8*, 38–55. [CrossRef]
33. Hsu, K.L.; Gao, X.G.; Sorooshian, S.; Gupta, H.V. Precipitation estimation from remotely sensed information using artificial neural networks. *J. Appl. Meteorol.* **1997**, *36*, 1176–1190. [CrossRef]
34. Sorooshian, S.; Hsu, K.-L.; Gao, X.; Gupta, H.V.; Imam, B.; Braithwaite, D. Evaluation of PERSIANN system satellite-based estimates of tropical rainfall. *Bull. Am. Meteorol. Soc.* **2000**, *81*, 2035–2046. [CrossRef]
35. Hong, Y.; Hsu, K.L.; Sorooshian, S.; Gao, X. Precipitation estimation from remotely sensed imagery using an artificial neural network cloud classification system. *J. Appl. Meteorol.* **2004**, *43*, 1834–1853. [CrossRef]
36. Ushio, T.; Kachi, M. Kalman Filtering Applications for Global Satellite Mapping of Precipitation (GSMaP). In *Satellite Rainfall Applications for Surface Hydrology*; Gebremichael, M., Hossain, F., Eds.; Springer: Dordrecht, The Netherlands, 2010.
37. Joyce, R.J.; Janowiak, J.E.; Arkin, P.A.; Xie, P. CMORPH: A method that produces global precipitation estimates from passive microwave and infrared data at high spatial and temporal resolution. *J. Hydrometeorol.* **2004**, *5*, 487–503. [CrossRef]
38. Huffman, G.J. README for Accessing Experimental Realtime TRMM Multi-Satellite Precipitation Analysis (TMPART) Data Sets. NASA Tech. Doc. 2015, 12. Available online: ftp://mesoa.gsfc.nasa.gov/pub/trmmdocs/rt/3B4XRT_README.pdf (accessed on 10 August 2019).
39. Funk, C.C.; Peterson, P.J.; Landsfeld, M.F.; Pedreros, D.H.; Verdin, J.P.; Sukla, S.; Husak, G.J.; Rowland, J.D.; Harrison, L.; Hoell, A.; et al. The climate hazards infrared precipitation with stations—A new environmental record for monitoring extremes. *Sci. Data* **2015**, *2*, 1–21. [CrossRef]
40. Beck, H.E.; Vergopolan, N.; Pan, M.; Levizzani, V.; van Dijk, A.I.J.M.; Weedon, G.P.; Brocca, L.; Pappenberger, F.; Huffman, G.J.; Wood, E.F. Global-scale evaluation of 22 precipitation datasets using gauge observations and hydrological modeling. *Hydrol. Earth Syst. Sci.* **2017**, *21*, 6201–6217. [CrossRef]
41. Dee, D.P.; Uppala, S.M.; Simmons, A.J.; Berrisford, P.; Poli, P.; Kobayashi, S.; Andrae, U.; Balmaseda, M.A.; Balsamo, G.; Bauer, P.; et al. The ERA-Interim reanalysis: Configuration and performance of the data assimilation system. *Q. J. R. Meteorol. Soc.* **2011**, *137*, 553–597. [CrossRef]
42. Kalnay, E. NCEP/NCAR 40-year reanalysis project. *Bull. Am. Meteorol. Soc.* **1996**, *77*, 437–472. [CrossRef]
43. Kanamitsu, M.; Ebisuzaki, W.; Woollen, J.; Yang, S.K.; Hnilo, J.J.; Fiorino, M.; Potter, G.L. NCEP–DOE AMIP-II reanalysis (R-2). *Bull. Am. Meteorol. Soc.* **2002**, *83*, 1631–1643. [CrossRef]
44. Kobayashi, S.; Ota, Y.; Harada, Y.; Ebita, A.; Moriya, M.; Onoda, H.; Onogi, K.; Kamahori, H.; Kobayashi, C.; Endo, H.; et al. The JRA-55 Reanalysis: General specifications and basic characteristics. *J. Meteorol. Soc. JPN* **2015**, *93*, 5–48. [CrossRef]
45. Molod, A.; Takacs, L.; Suarez, M.; Bacmeister, J. Development of the GEOS-5 atmospheric general circulation model: Evolution from MERRA to MERRA-2. *Geosci. Model. Dev.* **2015**, *8*, 1339–1356. [CrossRef]
46. Hersbach, H.; Bell, B.; Berrisford, P.; Hirahara, S.; Horányi, A.; Muñoz-Sabater, J.; Nicolas, J.; Peubey, C.; Radu, R.; Schepers, D.; et al. The ERA5 global reanalysis. *Q. J. R. Meteorol. Soc.* **2020**, *146*, 1999–2049. [CrossRef]

47. Bengtsson, L.; Hodges, K.; Esch, M.; Keenlyside, N.; Kornblueh, L.; Luo, J.; Yamagata, T. How may tropical cyclones change in a warmer climate? *Tellus A* **2007**, *59*, 539–561. [CrossRef]
48. Chen, G.; Iwasaki, T.; Qin, H.; Sha, W. Evaluation of the warm-season diurnal variability over East Asia in recent reanalyses JRA-55, ERA-Interim, NCEP CFSR, and NASA MERRA. *J. Clim.* **2014**, *27*, 5517–5537. [CrossRef]
49. Saha, S.; Moorthi, S.; Pan, H.-L.; Wu, X.; Wang, J.; Nadiga, S.; Tripp, P.; Kistler, R.; Wollen, J.; Berhringer, D.; et al. The NCEP Climate Forecast System Reanalysis. *Bull. Am. Meteorol. Soc.* **2010**, *91*, 1015–1058. [CrossRef]
50. Szczypta, C.; Calvet, J.C.; Albergel, C.; Balsamo, G.; Boussetta, S.; Carrer, D.; Lafont, S.; Meurey, C. Verification of the new ECMWF ERA-Interim reanalysis over France. *Hydrol. Earth Syst. Sci.* **2011**, *15*, 647–666. [CrossRef]
51. Anagnostou, E.N. Overview of overland satellite rainfall estimation for hydro-meteorological applications. *Surv. Geophys.* **2004**, *25*, 511–537. [CrossRef]
52. Hodges, K.I.; Lee, R.W.; Bengtsson, L. A comparison of extratropical cyclones in recent reanalyses ERA-Interim, NASA MERRA, NCEP CFSR, and JRA-25. *J. Clim.* **2011**, *24*, 4888–4906. [CrossRef]
53. Laviola, S.; Levizzani, V.; Cattani, E.; Kidd, C. The 183-wsl fast rain rate retrieval algorithm. part II: Validation using ground radar measurements. *Atmos. Res.* **2013**, *134*, 77–86. [CrossRef]
54. Lin, R.; Zhou, T.; Qian, Y. Evaluation of global monsoon precipitation changes based on five reanalysis datasets. *J. Clim.* **2014**, *27*, 1271–1289. [CrossRef]
55. Maggioni, V.; Sapiano, M.R.P.; Adler, R.F. Estimating uncertainties in high-resolution satellite precipitation products: Systematic or random error? *J. Hydrometeorol.* **2016**, *17*, 1119–1129. [CrossRef]
56. Urraca, R.; Huld, T.; Gracia-Amillo, A.; Martinez-De-Pison, F.J.; Kaspar, F.; Sanz-Garcia, A. Evaluation of global horizontal irradiance estimates from ERA5 and COSMO-REA6 reanalyses using ground and satellite-based data. *Sol. Energy* **2018**, *164*, 339–354. [CrossRef]
57. Zhao, D.M.; Fu, C.B. Comparisons of low-level circulation characteristics between ECHAM5/MPI-OM results and NCEP/NCAR re-analysis data in East Asia. *Atmos. Ocean. Sci. Lett.* **2010**, *3*, 189–194.
58. Sungmin, O.; Kirstetter, P.E. Evaluation of diurnal variation of GPM IMERG derived summer precipitation over the contiguous US using MRMS data. *Q. J. R. Meteorol. Soc.* **2018**, *144*, 270–281.
59. Omranian, E.; Sharif, H.O. Evaluation of the Global Precipitation Measurement (GPM) satellite rainfall products over the Lower Colorado River Basin, Texas. *J. Am. Water Resour.* **2018**, 1–17. [CrossRef]
60. Mahto, S.S.; Mishra, V. Does ERA-5 Outperform other reanalysis products for hydrologic applications in India? *J. Geophys. Res. Atmos.* **2018**, *124*, 9423–9441. [CrossRef]
61. Li, C.; Tang, G.; Hong, Y. Cross-evaluation of ground-based, multi-satellite and reanalysis precipitation products: Applicability of the triple collocation method across Mainland China. *J. Hydrol.* **2018**, *562*, 71–83. [CrossRef]
62. Huang, D.-Q.; Zhu, J.; Zhang, Y.-C.; Huang, Y.; Kuang, X.-Y. Assessment of summer monsoon precipitation derived from five reanalysis datasets over East Asia. *Q. J. R. Meteorol. Soc.* **2016**, *142*, 108–119. [CrossRef]
63. Bai, P.; Liu, X. Evaluation of five satellite-based precipitation products in two gauge-scarce basins on the Tibetan Plateau. *Remote Sens.* **2018**, *10*, 1316. [CrossRef]
64. Fan, B.; Luo, G.; Zhang, C.; Hu, Z.; Li, C.; Wang, Y.; Bai, L. Evaluation of summer precipitation of CFSR, ERA-Interim and MERRA reanalyses in Xinjiang. *Geophys. Res.* **2013**, *32*, 1602–1612, (In Chinese with English Abstract).
65. de Leeuw, J.; Methven, J.; Blackburn, M. Evaluation of ERA-Interim reanalysis precipitation products using England and Wales observations. *Q. J. R. Meteorol. Soc.* **2015**, *141*, 798–806. [CrossRef]
66. Derin, Y.; Anagnostou, E.N.; Berne, A.; Borga, M.; Boudevillain, B.; Buytaert, W.; Chang, C.-H.; Delrieu, G.; Hong, Y.; Hsu, Y.C.; et al. Multi-regional satellite precipitation products evaluation over complex terrain. *J. Hydrometeorol.* **2016**, *17*, 1817–1836. [CrossRef]
67. Guilloteau, C.; Roca, R.; Gosset, M. A Multiscale Evaluation of the Detection Capabilities of High-Resolution Satellite Precipitation Products in West Africa. *J. Hydrometeorol.* **2016**, *17*, 2041–2059. [CrossRef]
68. Lorenz, C.; Kunstmann, H. The hydrological in three state-of-the-art reanalysis: Intercomparison and performance analysis. *J. Hydrometeorol.* **2012**, *13*, 1397–1420. [CrossRef]
69. Yu, R.; Yuan, W.; Li, J. The asymmetry of rainfall process. *Chin. Sci. Bull.* **2013**, *58*, 1850–1856. [CrossRef]
70. Yu, R.; Yuan, W.; Li, J.; Fu, Y. Diurnal phase of late-night against late-afternoon of stratiform and convective precipitation in summer southern contiguous China. *Clim. Dyn.* **2010**, *35*, 567–576. [CrossRef]

71. Cheng, P.; Gao, L.; Zuo, X.; Zhong, F. Statistical analyses of spatial and temporal variabilities in total, daytime, and nighttime precipitation indices and of extreme dry/wet association with large-scale circulations of Southwest China, 1961–2016. *Atmos. Res.* **2019**, *219*, 166–182. [CrossRef]
72. Ghate, V.P.; Kollias, P. On the controls of daytime precipitation in the Amazonian dry season. *J. Hydrometeorol.* **2016**, *17*, 3079–3097. [CrossRef]
73. Wallace, J.M. Diurnal variations in precipitation and thunderstorm frequency over the conterminous united states. *Mon. Weather Rev.* **1975**, *103*, 406–419. [CrossRef]
74. Yu, R.; Xu, Y.; Zhou, T.; Li, J. Relation between rainfall duration and diurnal variation in the warm season precipitation over central eastern China. *Geophys. Res. Lett.* **2007**, *34*, L13703. [CrossRef]
75. Brown, K.; Kamruzzaman, M.; Beecham, S. Trends in sub-daily precipitation in Tasmania using regional dynamically downscaled climate projections. *J. Hydrol. Reg. Stud.* **2017**, *10*, 18–34. [CrossRef]
76. Lenderink, G.; van Meijgaard, E. Linking increases in hourly precipitation extremes to atmospheric temperature and moisture changes. *Environ. Res. Lett.* **2010**, *5*, 252–258. [CrossRef]
77. Lenderink, G.; Mok, H.Y.; Lee, T.C.; van Oldenborgh, G.J. Scaling and trends of hourly precipitation extremes in two different climate zones: Hong Kong and the Netherlands. *Hydrol. Earth Syst. Sci. Dis.* **2011**, *8*, 4701–4719. [CrossRef]
78. Liu, L.Y.; Ma, Z.-G. Intra-annual variability of diurnal cycle precipitation over china from 1960–2000. *Atmos. Ocean. Sci. Lett.* **2013**, *6*, 451–456.
79. Mao, J.Y.; Wu, G.X. Diurnal variations of summer precipitation over the Asian monsoon region as revealed by TRMM satellite data. *Sci. China Earth Sci.* **2012**, *55*, 554–566. [CrossRef]
80. Liu, X.; Zhang, M.; Wang, S.; Wang, J.; Zhao, P.; Zhou, P. Assessment of diurnal variation of summer precipitation over the Qilian Mountains based on an hourly merged dataset from 2008 to 2014. *J. Geogr. Sci.* **2017**, *27*, 326–336. [CrossRef]
81. Lin, C.; Liu, L.; Lin, W.; Bai, Y.; Qi, H.; Yang, H. Characteristics of summer precipitation diurnal variations in Hubei Province. *Trans. Atmos. Sci.* **2016**, *39*, 490–500, (In Chinese with English Abstract).
82. Han, Y.; Ma, Z.; Yang, Q.; Pan, Z. Changing Characteristics of Daytime and Nighttime Precipitation in Xinjiang under Global Warming. *Clim. Environ. Res.* **2014**, *19*, 763–772, (In Chinese with English Abstract).
83. Chen, F.; Gao, Y. Evaluation of precipitation trends from high-resolution satellite precipitation products over Mainland China. *Clim. Dyn.* **2018**, *51*, 3311–3331. [CrossRef]
84. Ren, Z.H.; Zhao, P.; Zhang, Q.; Zhang, Z.F.; Chen, Z. Quality control procedures for hourly precipitation data from automatic weather stations in China. *Meteorol. Mon.* **2010**, *36*, 123–132, (In Chinese with English Abstract).
85. The National Aeronautics and Space Administration (NASA) Shuttle Radar Topographic Mission (SRTM) 90m Digital Elevation Model (DEM) Digital Elevation Database. Available online: http://srtm.csi.cgiar.org/ (accessed on 7 July 2019).
86. Huang, R.; Chen, W.; Ding, Y.; Li, C. Studies on the monsoon dynamics and the interaction between monsoon and ENSO cycle. *Chin. J. Atmos. Sci.* **2003**, *27*, 484–502, (In Chinese with English Abstract).
87. Hsu, K.; Sellars, S.; Nguyen, P.; Braithwaite, D.; Chu, W. G-WADI PERSIANN-CCS GeoServer for extreme precipitation event monitoring. *Sci. Cold Arid Reg.* **2013**, *5*, 6–15.
88. Liu, Y.; Wu, Y.; Feng, Z.; Huang, X.; Wang, D. Evaluation of a Variety of Satellite Retrieved Precipitation Products Based on Extreme Rainfall in China. *Trop. Geogr.* **2007**, *37*, 417–433, (In Chinese with English Abstract).
89. Shen, Y.; Xiong, A.; Wang, Y.; Xie, P. Performance of high-resolution satellite precipitation products over China. *J. Geophys. Res. Atmos.* **2010**, *115*, D02114. [CrossRef]
90. Wang, Y.; Xie, X.; Meng, S.; Wu, D.; Chen, Y.; Jiang, F.; Zhu, B. Magnitude agreement, occurrence consistency, and elevation dependency of satellite-based precipitation products over the Tibetan Plateau. *Remote Sens.* **2020**, *12*, 1750. [CrossRef]
91. Xiao, S.; Xia, J.; Zou, L. Evaluation of multi-satellite precipitation products and their ability in capturing the characteristics of extreme climate events over the Yangtze River Basin, China. *Water* **2020**, *12*, 1179. [CrossRef]
92. Qin, Y.; Chen, Z.; Shen, Y.; Zhang, S.; Shi, R. Evaluation of Satellite Rainfall Estimates over the Chinese Mainland. *Remote Sens.* **2014**, *6*, 11649–11672. [CrossRef]

93. Ngo-Duc, T.; Matsumoto, J.; Kamimera, H.; Bui, H.-H. Monthly adjustment of Global Satellite Mapping of Precipitation (GSMaP) data over the VuGia–ThuBon River Basin in Central Vietnam using an artificial neural network. *Hydrol. Res. Lett.* **2013**, *7*, 85–90. [CrossRef]
94. Try, S.; Tanaka, S.; Tanaka, K.; Sayama, T.; Oeurng, C.; UK, S.; Takara, K.; Hu, M.; Han, D. Comparison of gridded precipitation datasets for rainfall-runoff and inundation modeling in the Mekong River Basin. *PLoS ONE* **2020**, *15*, e0226814. [CrossRef]
95. Fallah, A.; Rakhshandehroo, G.R.; Berg, P.; Sungmin, O.; Orth, R. Evaluation of precipitation datasets against local observations in southwestern Iran. *Int. J. Climatol.* **2020**, *40*, 4102–4116. [CrossRef]
96. Nogueira, M. Inter-comparison of ERA-5, ERA-Interim and GPCP rainfall over the last 40 years: Process-based analysis of systematic and random differences. *J. Hydrol.* **2020**, *583*, 124632. [CrossRef]
97. Nogueira, M. The multi-scale structure of atmospheric energetic constraints on globally averaged precipitation. *Earth Syst. Dyn.* **2019**, *10*, 219–232. [CrossRef]
98. Stephens, G.L.; Ellis, T.D. Controls of global-mean precipitation increases in global warming GCM experiments. *J. Clim.* **2008**, *21*, 6141–6155. [CrossRef]
99. Ma, L.; Zhang, T.; Frauenfeld, O.W.; Ye, B. Evaluation of precipitation from the ERA-40, NCEP-1, and NCEP-2 reanalyses and CMAP-1, CMAP-2, and GPCP-2 with ground-based measurements in China. *J. Geophys. Res. Atmos.* **2009**, *114*, D09105. [CrossRef]
100. Tang, D.; Ma, C.; Wang, Y.; Xu, X. Multiscale evaluation of NCEP and CRUNCEP data sets at 90 large U.S. cities. *J. Geophys. Res. Atmos.* **2017**, *122*, 7433–7444. [CrossRef]
101. Hua, W.; Zhou, L.; Nicholson, S.E.; Chen, H.; Qin, M. Assessing reanalysis data for understanding rainfall climatology and variability over Central Equatorial Africa. *Clim. Dyn.* **2019**, *53*, 5139. [CrossRef]
102. Trenberth, K.E.; Fasullo, J.T.; Mackaro, J. Atmospheric moisture transports from ocean to land and global energy flows in reanalyses. *J. Clim.* **2011**, *24*, 4907–4924. [CrossRef]
103. Zhang, L.; Kumar, A.; Wang, W. Influence of changes in observations on precipitation: A case study for the Climate Forecast System Reanalysis (CFSR). *J. Geophys. Res. Atmos.* **2012**, *117*, D08105. [CrossRef]
104. Hamal, K.; Sharma, S.; Khadka, N.; Baniya, B.; Ali, M.; Shrestha, M.S.; Xu, T.; Shrestha, D.; Dawadi, B. Evaluation of MERRA-2 Precipitation Products Using Gauge Observation in Nepal. *Hydrology* **2020**, *7*, 40. [CrossRef]
105. Zandler, H.; Haag, I.; Samimi, C. Evaluation needs and temporal performance differences of gridded precipitation products in peripheral mountain regions. *Sci. Rep.* **2019**, *9*, 1–15. [CrossRef] [PubMed]
106. Devine, K.A.; Mekis, É. Field accuracy of Canadian rain measurements. *Atmos. Ocean.* **2008**, *46*, 213–227. [CrossRef]
107. Lanza, L.G.; Vuerich, E. The WMO Field Intercomparison of Rain Intensity Gauges. *Atmos. Res.* **2009**, *94*, 534–543. [CrossRef]
108. Pollock, M.D.; O'Donnell, G.; Quinn, P.; Dutton, M.; Black, A.; Wilkinson, M.E.; Colli, M.; Stagnaro, M.; Lanza, L.G.; Lewis, E.; et al. Quantifying and mitigating wind-induced undercatch in rainfall measurements. *Water Resour. Res.* **2018**, *54*, 3863–3875. [CrossRef]
109. Shedekar, V.S.; King, K.W.; Fausey, N.R.; Soboyejo, A.B.O.; Harmel, R.D.; Brown, L.C. Assessment of measurement errors and dynamic calibration methods for three different tipping bucket rain gauges. *Atmos. Res.* **2016**, *178*, 445–458. [CrossRef]
110. Sieck, L.C.; Burges, S.J.; Steiner, M. Challenges in obtaining reliable measurements of point rainfall. *Water Resour. Res.* **2007**, *43*, W01420. [CrossRef]
111. Wang, X.; Xu, H.; Qian, B.; Feng, Y.; Mekis, E. Adjusted daily rainfall and snowfall data for Canada. *Atmos. Ocean.* **2017**, *55*, 155–168. [CrossRef]
112. Groisman, P.Y.; Koknaeva, V.V.; Belokrylova, T.A.; Karl, T.R. Overcoming biases of precipitation measurement: A history of the USSR experience. *Bull. Am. Meteorol. Soc.* **1991**, *72*, 1725–1732. [CrossRef]
113. Strangeways, I. Improving precipitation measurement. *Int. J. Climatol.* **2004**, *24*, 1443–1460. [CrossRef]
114. Adam, J.C.; Lettenmaier, D.P. Adjustment of global gridded precipitation for systematic bias. *J. Geophys. Res. Atmos.* **2003**, *108*, 4257. [CrossRef]
115. Kochendorfer, J.; Nitu, R.; Wolff, M.A.; Mekis, E.; Rasmussen, R.; Baker, B.; Earle, M.E.; Reverdin, A.; Wong, K.; Simith, C.D.; et al. Analysis of single-Alter-shielded and unshielded measurements of mixed and solid precipitation from WMO-SPICE. *Hydrol. Earth Syst. Sci.* **2017**, *21*, 3525–3542. [CrossRef]

116. Leeper, R.D.; Kochendorfer, J. Evaporation from weighing precipitation gauges: Impacts on automated gauge measurements and quality assurance methods. *Atmos. Meas. Tech.* **2015**, *8*, 2291–2300. [CrossRef]
117. Stewart, R.D.; Hut, R.; Rupp, D.; Gupta, H.; Selker, J.S. A resonating rainfall and evaporation recorder. *Water Resour. Res.* **2012**, *48*, W08601. [CrossRef]
118. Yang, D.; Ohata, T. A bias-corrected Siberian regional precipitation climatology. *J. Hydrometeorol.* **2001**, *2*, 122–139. [CrossRef]
119. Buishand, T. Some methods for testing the homogeneity of rainfall records. *J. Hydrol.* **1982**, *58*, 11–27. [CrossRef]
120. García-Marín, A.P.; Estévez, J.; Morbidelli, R.; Saltalippi, C.; Ayuso-Muñoz, J.L.; Flammini, A. Assessing inhomogeneities in extreme annual rainfall data series by multifractal approach. *Water* **2020**, *12*, 1030. [CrossRef]
121. Liu, W.; Fu, Z.; Chen, X.; Qu, J.; Wang, J.; Peng, X. Inhomogeneity of precipitation and its influencing factors in Northwest China from 1961 to 2015. *Theor. Appl. Climatol.* **2019**, *138*, 1831–1844. [CrossRef]
122. Peterson, T.C.; Easterling, D.R. Creation of homogeneous composite climatological reference series. *Int. J. Climatol.* **1994**, *14*, 671–680. [CrossRef]
123. Wu, Y.; Zhang, Z.; Huang, Y.; Jin, Q.; Chen, X.; Chang, J. Evaluation of the GPM IMERG v5 and TRMM 3B42 v7 Precipitation Products in the Yangtze River Basin, China. *Water* **2019**, *11*, 1459. [CrossRef]
124. Qiu, Q.; Liu, J.; Tian, J.; Jiao, Y.; Li, C.; Wang, W.; Yu, F. Evaluation of the radar QPE and rain gauge data merging methods in Northern China. *Remote Sens.* **2020**, *12*, 363. [CrossRef]
125. Thakur, M.K.; Kumar, T.V.L.; Rao, K.K.; Barbosa, H.; Rao, V.B. A new perspective in understanding rainfall from satellites over a complex topographic region of India. *Sci. Rep.* **2019**, *9*, 15610. [CrossRef] [PubMed]
126. Steiner, M.; Smith, J.A.; Burges, S.J.; Alonso, C.V.; Darden, R.W. Effect of bias adjustment and rain gauge data quality control on radar rainfall estimation. *Water Resour. Res.* **1999**, *35*, 2487–2503. [CrossRef]
127. Tang, G.; Behrangi, A.; Long, D.; Li, C.; Hong, Y. Accounting for spatiotemporal errors of gauges: A critical step to evaluate gridded precipitation products. *J. Hydrol.* **2018**, *559*, 294–306. [CrossRef]
128. Villarini, G.; Mandapaka, P.V.; Krajewski, W.F.; Moore, R.J. Rainfall and sampling uncertainties: A rain gauge perspective. *J. Geophys. Res. Atmos.* **2008**, *113*, D11102. [CrossRef]
129. Wood, S.J.; Jones, D.A.; Moore, R.J. Accuracy of rainfall measurement for scales of hydrological interest. *Hydrol. Earth Syst. Sci.* **2000**, *4*, 531–543. [CrossRef]